Oscillatory climate modes in the Eastern Mediterranean and their synchronization with the North Atlantic Oscillation

Yizhak Feliks[1] Michael Ghil[2,3] and Andrew W. Robertson[4]

Department of Atmospheric & Oceanic Sciences and Institute of Geophysics & Planetary Physics, University of California, Los Angeles, USA

Revised Version, 5 January 2010

[1]Permanent address: Department of Mathematics, Israel Institute of Biological Research, Ness Ziona, Israel
[2]Additional affiliation: Geosciences Department and Laboratoire de Météorologie Dynamique (CNRS and IPSL), Ecole Normale Supérieure, Paris, France.
[3]Corresponding author, E-mail: ghil@atmos.ucla.edu .
[4]Permanent address: International Research Institute for climate and society (IRI), Monell Building, Room 230, P. O. Box 1000, Palisades, NY 10964-8000, USA

Abstract

Oscillatory climatic modes over the North Atlantic, Ethiopian Plateau and Eastern Mediterranean were examined in instrumental and proxy records from these regions. Aside from the well-known North Atlantic Oscillation (NAO) index and the Nile River water-level records, we study for the first time an instrumental rainfall record from Jerusalem and a tree-ring record from the Golan Heights.

The teleconnections between the regions were studied in terms of synchronization of chaotic oscillators. We modify standard methods for studying synchronization among such oscillators by combining them with advanced spectral methods, including singular spectrum analysis. The resulting cross-spectral analysis quantifies the strength of the coupling together with the degree of synchronization.

A prominent oscillatory mode with a 7–8-year period is present in all the climatic indices studied here and is completely synchronized with the North Atlantic Oscillation. An energy analysis of the synchronization raises the possibility that this mode originates in the North Atlantic. Evidence is discussed for this mode being induced by the 7–8-year oscillation in the position of the Gulf Stream front. A mechanism for the teleconnections between the North Atlantic, Ethiopian Plateau and Eastern Mediterranean is proposed, and implications for interannual-to-decadal climate prediction are discussed.

1. Introduction

Interannual and interdecadal oscillations have been found in many variables and parts of the Earth's climate system; see Ghil and Vautard (1991), Dettinger et al. (1995), Plaut et al. (1995), Unal and Ghil (1995), Moron et al. (1998), and many others. These oscillations are usually correlated across large regions, on the order of thousands of kilometers, through "teleconnections" (Wallace and Gutzler, 1981; Barnston and Livezey, 1987) that have been attributed to several causes, including the propagation of atmospheric Kelvin and Rossby waves, changes in thermally direct circulations, intrinsic modes of atmospheric variability, and changes in the oceans' wind-driven or thermohaline circulation. The terms "teleconnection" and "oscillation" have often been used synonymously in meteorology, ever since the discovery of the North Atlantic, North Pacific and Southern Oscillations by G. Walker and associates (e.g., Walker and Bliss, 1932, 1937); in these cases, the term "oscillation" was used merely to describe large-scale seesaw patterns in sea level pressures.

These pioneering studies did not imply the presence of distinct spectral peaks, although Walker (1931) did hint at their presence in the Southern Oscillation (SO). We now know that the SO is strongly coupled to El Niño (EN) sea surface temperature anomalies to form ENSO, which exhibits pronounced interannual periods (Philander, 1990; Jiang et al., 1995a) and has near-global climate impacts through atmospheric teleconnections (Hoskins and Karoly, 1981; Ropelewski and Halpert, 1987; Chiang and Sobel, 2002; Lintner and Chiang, 2007). In the mid-latitudes, the best-known oscillatory patterns are the North Atlantic Oscillation (NAO: Rogers, 1990; Hurrell, 1995) and the Pacific Decadal Oscillation (Mantua et al., 1997; Chao et al., 2000), while the tropics are

dominated by ENSO (Rasmusson and Carpenter, 1982; Philander, 1990).

We examine here interannual and interdecadal climate variability over the Eastern Mediterranean during the last two centuries. Several instrumental and proxy records longer than 100 years exist for different sites in the region. The records we analyze include precipitation records from Jerusalem, as well as tree-ring records from the Golan Heights (Feliks, 1968), and the Nile River flow records previously analyzed by Kondrashov et al. (2005). We use advanced spectral methods, including singular-spectrum analysis (SSA), to find the most significant oscillatory modes in these climatic records (Ghil et al., 2002a), and relate them to similar modes over the North Atlantic.

We concentrate therewith on the Eastern Mediterranean and on potential teleconnections with the North Atlantic Ocean and the Ethiopian Plateau. Previous teleconnection studies were based on correlations between climatic time series from the regions of interest (Wallace and Gutzler, 1981); often the correlations were no larger than 0.6 and they did not clarify in which frequency band the teleconnection under investigation was most active.

The commonalities between the well-documented records of the NAO index and the records representing the focus area of our paper are considered here from the point of view of synchronization between chaotic oscillators (Rosenblum et al., 1996; Duane, 1997; Boccaletti et al., 2002; Osipov et al., 2003; Duane and Tribbia, 2004). From this point of view, each regional climatic index may be considered as a chaotic oscillator representing the regional dynamics of local climate; teleconnections then arise as a coupling in space between locations. Our synchronization analysis differs from that of previous studies inasmuch as we use multi-channel SSA (M-SSA) to examine cross-

spectral properties of the climate records from different regions, and focus therewith on studying the commonalities between oscillatory components of the records. Based on this preliminary analysis, significant oscillatory modes are reconstructed and we apply the synchronization analysis to these modes. Such an approach allows us to identify which regions are teleconnected and, using a novel energy-ratio criterion, we can determine the strength of the coupling and the region in which each oscillatory mode arises.

In section 2, our modified synchronization analysis is described and it is illustrated by its application to a system of two coupled Rössler (1976) oscillators. In section 3, we provide a short analysis of each climate record separately, while in section 4 we examine the synchronization between the records from different regions and consider the mechanism of this synchronization. Concluding remarks appear in section 5.

2. Synchronization of chaotic time series

2.1 Basic methodology and its modification

We follow the overall approach of Rosenblum et al. (1996) and Osipov et al. (2003) in our analysis of the synchronization between two chaotic time series, and will present some new concepts and tools after summarizing their approach. First, these authors, following Gabor (1946) and Panter (1965), define an analytic signal $\psi(t)$ associated with a given time series $x(t)$. This analytic signal is the complex-valued time series

$$\psi(t) = x(t) + iy(t), \tag{1a}$$

where $i = \sqrt{-1}$ is the imaginary unit and

$$y(t) = \pi^{-1} PV \int_{-\infty}^{\infty} \frac{x(s)}{s-t} ds \tag{1b}$$

is the Hilbert transform of $x(t)$, $y(t) = H[x(t)]$. The instantaneous amplitude $A(t)$ and phase $\phi(t)$ of the analytic signal $\psi(t)$ are defined by the polar representation of Eq. (1a),

$$\psi(t) = A(t)\exp[i\phi(t)], \tag{1c}$$

where

$$A(t) = [x^2(t) + y^2(t)]^{1/2}, \qquad \phi(t) = \arctan[y(t)/x(t)]. \tag{2a,b}$$

Two signals, $x_1(t)$ and $x_2(t)$, are said to be synchronized when the phase difference $d(t) = \phi_1(t) - \phi_2(t)$ between the two does not grow with time. Note that the phase angle $\phi(t)$ is allowed to increase beyond 2π.

The integral in Eq. (1b) is ill-posed, and thus the Hilbert transform $y(t) = H[x(t)]$ of $x(t)$ is often estimated by applying a discrete Fourier transform to $x(t)$, setting all negative frequencies to zero, and transforming it back into the time domain. Marple (1999) discussed the mathematical properties of an analytic signal, as well as its numerical estimation by such a procedure. For each sine component $x(t) = \sin(t)$, the Hilbert transform returns its cosine counterpart $H[x(t)] = -\cos(t)$; Eq. (2b) thus yields the correct phase, but with the opposite sign, in this special case. Sometimes one uses, therefore, $-H$ as a more convenient transform; since we will only need to consider phase differences here, we keep H as our transform, with the plus sign.

There is, however, a hitch: in general, the Hilbert transform is numerically ill posed, i.e. $H[x(t)]$ depends sensitively on small errors in $x(t)$. Intuitively, for a broad-band signal one might get a multitude of phases that are hard to separate from each other, rather than a single phase.

The climate records we consider in this paper are short, 100–200 years or less, and there are only about 4–10 data points per period of interest. Hence the Marple (1999)

method for the calculation of the Hilbert transform does not yield satisfactory results either. Moreover, it is well-nigh impossible to test over just a very few full periods whether the phase difference $d(t)$ between two nearly equal periodicities in the time series $x_1(t)$ and $x_2(t)$ does increase with time or not. We use therefore a different approach, in order to find the phase and amplitude of an arbitrary signal; this approach has been tested extensively and found to be useful in studying oscillatory modes present in short and noisy climate records (Ghil et al., 2002a).

The instantaneous phase $\phi_i(t)$ of each signal $\psi_i(t)$ is given, following Plaut and Vautard (1994) and Moron et al. (1998), by

$$\phi_i(t) = \arctan[x_i'(t)/ x_i(t)], \tag{3}$$

where $x'(t)$ is the time derivative of $x(t)$, while the instantaneous amplitude $A_i(t)$ is given by the local extremum (maximum or minimum) of the signal that is nearest to the epoch t. The key insight of these authors was precisely to only treat in this way the narrow-band signals obtained by SSA pre-filtering, namely the reconstructed components (RCs) associated with an oscillatory mode. Since the RCs are such narrow-band, modulated signals, the Bedrosian (1963) theorem justifies the application of the Hilbert transform to them, in order to obtain a well-defined, unique phase.

The synchronization between two signals is measured by the standard deviation σ of the instantaneous phase difference between the two time series,

$$\sigma^2 = <(d(t) - < d(t)>)^2>, \tag{4a}$$

and the correlation $cor(A_1, A_2)$ between the instantaneous amplitudes:

$$cor(A_1, A_2) =< A_1 A_2 > / \sqrt{< A_1^2 >< A_2^2 >}\ , \tag{4b}$$

where < > denotes time averaging. Following Osipov et al. (2003), one can identify three types of synchronization in chaotic time series, which we label as follows:

(F) synchronization of the frequencies alone, i.e. *frequency locking*; in this case

$$0.5 = \sigma_0 < \sigma < \infty;$$

(FP) synchronization of the phases as well, i.e. *phase locking*,

$$\sigma < \sigma_0 = 0.5;$$

and finally

(FPA) *complete synchronization*, including both phases and amplitudes, so that

$$cor(A_1, A_2) \approx 1.$$

Frequency locking (F) does not imply phase locking (FP), as can be easily seen from adding any perturbation with a broad-band, continuous spectrum — whether random or deterministically chaotic, like any variable of the Lorenz (1963) model — to one of two harmonic oscillators having the same frequency. The threshold $\sigma_0 = 0.5$ in (FP) is fairly arbitrary, but clearly much smaller than π. When examining the coupling of two Rössler oscillators, Rosenblum et al. (1996) found that, as the strength of the coupling increases, the degree of synchronization increases as well, from (F) to (FP) and on to (FPA).

The difficulty in estimating the quantities defined in Eqs. (1)–(4) and used in the definitions of synchronization (F)–(FPA) resides in the essential ill-posedness of the differentiation of chaotic time series, especially in the presence of measurement and sampling noise (Maraun and Kurths, 2004). This difficulty has given rise to several different techniques for estimating the phase and amplitude associated with a given time series. To obtain smooth and reliable estimates of these quantities, we apply two advanced, well-documented spectral methods to find the oscillatory modes shared by the

two time series, namely SSA and, for verification purposes, the multi-taper method (MTM) of Thomson (1982). These two methods, along with additional ones, are available in the freeware SSA-MTM Toolkit at http://www.atmos.ucla.edu/tcd/ssa/.

Multi-channel SSA (M-SSA) is an extension of SSA to several time series, with each "channel" corresponding to one of the scalar time series of interest (Broomhead and King, 1986; Keppenne and Ghil, 1993; Plaut and Vautard, 1994; Ghil et al., 2002a). The method essentially diagonalizes the lag-covariance matrix associated with the vector time series whose components are the channels. The eigenvectors of this matrix are the space-time empirical orthogonal functions (ST-EOFs) and projection onto them yields the corresponding principal components.

The entire vector time series or parts thereof that correspond to trends, oscillatory modes or noise can be reconstructed by using linear combinations of these principal components and ST-EOFs, which provide the spatio-temporal RCs. A statistical significance test against red noise is performed by comparing the projection of the data onto a given ST-EOF for each channel with the corresponding projections of a large ensemble of red-noise surrogates (Allen and Robertson, 1996; Ghil et al., 2002a).

We thus assess synchronization of a pair of records by applying a two-channel M-SSA, with each channel corresponding to one of the two records; each record is nondimensionalized by its standard deviation. Shared signals that are statistically significant at the 95% level are analyzed further to quantify their degree of synchronization. The standard deviation σ of the instantaneous phase difference between them is computed via (4a), using Eq. (3) to estimate each instantaneous phase.

2.2 Application to coupled Rössler oscillators

In this section, we illustrate the modified synchronization analysis method described in section 2.1 above by applying it to a system of two coupled Rössler (1976) oscillators, and examine the route to synchronization in the parameter range studied by Rosenblum et al. (1996). The Rössler oscillator provides a simple chaotic-system analog of regional climate. Its orbits spiral around a single pole, rather than the two poles of the Lorenz (1963) model's "butterfly," with its two wings; it is thus simpler to define instantaneous phase than in the "bipolar" Lorenz model.

The Rössler oscillator, sometimes called simply the "Rösselator" for short, is also very popular in studies of deterministic chaos. For instance, Janjarasjitt and Loparo (2008) studied recently a coupled system of two such oscillators with distinct parameters, while Brunnet et al. (1994) investigated the collective behavior of a two-dimensional square lattice of identical Rössler oscillators. The latter is a more sophisticated counterpart of the Lorenz (1991, 1996) models; in both cases, E. N. Lorenz studied a one-dimensional, regularly spaced lattice of oscillators. Either the Lorenz (1991, 1996) models or the Brunnet et al. (1994) model can serve for the conceptual investigation of teleconnections among local or regional climates.

The equations of the coupled Rössler system are, for i = 1, 2,

$$\begin{aligned} \frac{dx_{1,2}}{dt} &= -\omega_{1,2} y_{1,2} - z_{1,2} + C(x_{2,1} - x_{1,2}) \\ \frac{dy_{1,2}}{dt} &= \omega_{1,2} x_{1,2} + 0.15 y_{1,2} \qquad , \qquad (5) \\ \frac{dz_{1,2}}{dt} &= 0.2 + z_{1,2}(x_{1,2} - 10) \end{aligned}$$

where ω_1 = 1.015 and ω_2 =0.985 are the two angular frequencies of the uncoupled oscillators, and C is the coupling parameter between the two oscillators. We used the

Adams-Bashforth scheme to integrate Eqs. (5) with a time step of $\delta t = 0.01$, and stored the first components $x_1(t)$ and $x_2(t)$ of the two oscillators every $\Delta t = 0.5$ time units, i.e. every 50 time steps. The synchronization analysis was carried out on the two model-generated time series $x_1(t)$ and $x_2(t)$ in the time interval $t = 1000$–4000.

Applying the synchronization criteria of Eqs. (1)–(4) to the two time series $x_1(t)$ and $x_2(t)$ we find that, for $C < 0.027$, the two time series are not synchronized at all: the standard deviation σ of the phase differences is large and the amplitude correlation is quite small; see Table 1 and Fig. 1a ($C = 0.017$). For $C = 0.027$, the standard deviation is $\sigma = 7.9$ over a time interval of 3000 time units, which is finite but already quite large (in particular larger than π) and actually tends to infinity as the time interval increases to infinity (not shown), while the amplitude correlation is small, $cor(A_1, A_2) = 0.08$, and does stay so as the interval increases.

When increasing the coupling strength to $C = 0.035$, the standard deviation of the phase difference drops to $\sigma = 0.21$ and changes but little as the time interval increases; thus both the frequencies and phases of the two oscillators are synchronized. On the other hand, the amplitude correlation only reaches 0.24, cf. Fig. 1b ($C = 0.035$); so the synchronization type is only (FP), and not (FPA). From Fig. 1b, one sees in fact that — while the two time series keep a constant lead-lag relationship, unlike in Fig. 1b — the amplitude evolutions of the two series do not match. These results agree with those of Rosenblum et al. (1996).

Next we compute the cross-spectra of x_1 and x_2, by applying M-SSA with two channels, and using a window width of $M = 60\Delta t = 30$ time units (Ghil et al., 2002a). The RC of an oscillatory mode associated with a given pair (i, i+1) of ST-EOFs will be

denoted by $RC^{(i,\ i+1)}$; the corresponding components will be called $RC^{(i,\ i+1)}x_1$ for channel x_1 and $RC^{(i,\ i+1)}x_2$ for channel x_2, and the energy (variance) in each of the two RC components will be identified as $E(RC^{(i,\ i+1)}x_1)$ and $E(RC^{(i,\ i+1)}x_2)$, respectively.

For C = 0.0, the oscillators are not coupled and we obtain five significant eigenvalues of the lag-covariance matrix: 2 eigenvalues equal to 0.168, 2 equal to 0.162, and one equal to 0.202; the significance is established with respect to the noise present in the two time series $x_1(t)$ and $x_2(t)$, due to the interaction between the numerical truncation and the nonlinearity (Henrici, 1963; Isaacson and Keller, 1966). The RC associated with the first ST-EOF pair, $RC^{(1,2)}$, captures 51% of the variance and has energy only in $RC^{(1,2)}x_2$. The second significant pair of RCs, $RC^{(3,4)}$, captures 35% of the variance and has energy only in $RC^{(3,4)}x_1$. There is no oscillatory mode that contains energy in both RCx_1 and RCx_2, as expected for the uncoupled system; the two pairs of eigenvalues simply correspond to the values of the frequencies ω_1 and ω_2. The RCs associated with the first four modes, $RC^{(1-4)}$, contain 51% + 35% = 86% of the variance. The amplitude correlation between $RC^{(1-4)}x_1$ and $RC^{(1-4)}x_2$ is 0.12, about the same as the amplitude correlation between the complete time series $x_1(t)$ and $x_2(t)$.

By increasing the coupling strength between the two oscillators, the system changes gradually as follows: (a) The five significant eigenvalues become closer in value and merge eventually; for C = 0.035, when the system experiences phase synchronization (see again Table 1), these five eigenvalues have completely merged (not shown). (b) The variance of the $RC^{(1,2)}$ oscillatory mode increases and that of the $RC^{(3,4)}$ mode decreases as C increases; see columns 2 and 3 of Table 1. (c) The energy ratio $\varepsilon_{12} = E(RCx_1)/E(RCx_2)$ between the two components of the $RC^{(1,2)}$ oscillatory mode increases

and tends to 1.0 as C increases (column 4 of Table 1); the energy ratio $\varepsilon_{34} = E(\mathrm{RC}x_1)/E(\mathrm{RC}x_2)$ of the $\mathrm{RC}^{(3,4)}$ oscillatory mode decreases (from infinity) and also tends to unity as C increases (not shown). The ratio ε_{34} for the oscillatory mode associated with the second pair is almost equal to that associated with the first pair. (d) The standard deviation of the phase difference σ decreases as C increases (column 5 of Table 1) and we use it to measure the phase synchronization of the system.

The piling up of the variance in the RC pair (1,2) is clearly of the essence in the synchronization process. The equalization of the energy ratios ε_{12} and ε_{34} between the two components of the $\mathrm{RC}^{(1,2)}$ mode and the $\mathrm{RC}^{(3,4)}$ mode, respectively, may be due to the symmetry of the coupled system, with two identical Rössler oscillators being involved.

Increasing C from 0.027 to 0.035, the energy in the $\mathrm{RC}^{(1,2)}$ mode increases from 86% to 93% and that of the $\mathrm{RC}^{(3,4)}$ mode decreases from 9% to 1%, while σ changes from 7.9 to 0.21 (see again Table 1 and Fig. 1), and thus the synchronization type of the system is (FP) for C = 0.035. Increasing C further to 0.12 increases the amplitude correlation from 0.24 to 0.96 (column 6 of Table 1, and Fig. 1c, with C = 0.12) and now the system's synchronization is complete, i.e., of (FPA) type; the two time series are now visually indistinguishable (Fig. 1c).

Thus our conclusions about the synchronization type in the coupled Rössler oscillator pair, as a function of the coupling strength, agree with those of Osipov et al. (1993) and Rosenblum et al. (1996). Their criteria, though, relied on the Lyapunov spectrum, while ours rely on M-SSA. The latter criteria seem more robust in the analysis of large systems and for short and noisy time series, like those available in climate dynamics and the geosciences in general: reliable calculation of Lyapunov exponents

requires very long and relatively clean time series. In order to show that the results for the coupled Rössler oscillators in this section are not an artifact of the M-SSA analysis, we investigate in appendix A two even simpler synthetic-data examples.

Along the route to synchronization between the coupled Rössler oscillators, and for all values of $C > 0$, the synchronization between the components RCx_1 and RCx_2 that belong to the same oscillatory pair is of complete (FPA) type, since the corresponding σ is quite small, $\sigma \ll 1$, and the amplitude correlation is about 1. A difference between the two components persists, though, for low coupling strength and is manifest in the energy ratio $E(\mathrm{RC}x_1)/E(\mathrm{RC}x_2)$: this ratio tends to unity for strong coupling and tends to zero (respectively infinity) as $C \to 0$. Therefore, in the analysis of the cross-spectra of several pairs of climatic records, we will examine the ratio $\varepsilon = E(\mathrm{RC}x_1)/E(\mathrm{RC}x_2)$ to identify the coupling strength in significant frequency bands, in addition to the synchronization type.

Tentatively, the results for the coupled Rössler oscillators suggest that the direction of influence can be inferred from the energy ratio as follows. When the energy ratio is close to unity the direction of influence cannot be inferred via this criterion. For weak coupling, $|E(\mathrm{RC}x_1)/E(\mathrm{RC}x_2)| \ll 1$, due to the much larger energy in $\mathrm{RC}^{(1,2)}x_2$, the direction of influence in the first pair is from x_2 to x_1. The opposite direction of influence is obtained for the second pair. As the coupling increases, so does the degree of synchronization, while the energy ratio between the first and second component within each pair increases but is still less than unity; in this case, we can still identify the direction of influence, in the presence of strong coupling — i.e., for synchronization of the (FP) or (FPA) type.

In the following we analyze the synchronization between different climatic records for the last one-to-two centuries; the records stem from the North Atlantic, Eastern Mediterranean and North Africa. The methodology used is the one described so far. In this perspective, the climate system can be interpreted as being represented by a large number of coupled oscillators (Ghil and Childress, 1987; Lorenz, 1991, 1996). Significant modes that have similar periods and are found in distinct regions (Ghil et al., 2002a) may then be due to the coupling of such oscillators. We thus test not only (i) the degree of synchronization, but also (ii) the strength of the coupling, by evaluating the ratio $\varepsilon = E(\mathrm{RC}x_1)/E(\mathrm{RC}x_2)$ for a given oscillatory mode of the cross-spectral analysis, and also, albeit tentatively, (iii) the direction of influence.

3. The climatic records

In this section we examine the spectral properties of the individual climatic records from the Eastern Mediterranean, Ethiopian Plateau, and the North Atlantic. The climate records from the Eastern Mediterranean are instrumental precipitation records from Jerusalem, and tree-ring records from the Golan Heights. The proxy records associated with the Ethiopian Plateau are the high-water records of the Nile River. For the North Atlantic we use the well-known NAO index.

Single-channel SSA is applied to each time series in turn. Statistical significance is assessed using Monte-Carlo SSA (MC-SSA; Allen and Smith, 1996) against a red-noise null-hypothesis constructed from a surrogate data ensemble of 100 series, each with the same variance and lag-one autocorrelation as the original record.

The surrogate time series (Allen and Smith, 1996) were produced by projecting the first 10 principal components of the SSA analysis onto the basis vectors of a red-noise

process. In order to check the robustness of the peaks identified via SSA, the Mann and Lees (1996) version of the MTM method (see also Ghil et al., 2002a, and the documentation available at http://www.atmos.ucla.edu/tcd/ssa/) was also applied, using 3 tapers and a spectral resolution of 0.03 cycles/year. In this MTM version, statistical significance is also assessed against a red-noise background, and associated 50%, 90%, 95%, and 99% significance levels are computed. A summary of the modes identified as statistically significant at the 95% level using both MC-SSA and MTM are given in Table 2, along with the percentage of variance (of the detrended time series) captured by the corresponding SSA mode.

3.1. Jerusalem precipitation record

The annual mean precipitation records from Jerusalem cover the 133 years from 1861 to 1994; see Fig. 2c. D. Ashbel compiled the records for the years 1861–1964, and the Israel Meteorological Service those for 1965–1994. Dan Yakir from the Weizmann Institute of Science communicated these so-far unpublished records to us.

To concentrate on the interannual periodicities in these precipitation records, as well as in the other records discussed below, we first removed the lowest-frequency components, including the nonlinear trend (Ghil et al., 2002a). In the rainfall records, the three components that fall in this category are (1,2,3), when carrying out the SSA analysis with a window width of M = 45 year. Next we applied MC-SSA with a window of M = 40 year to the detrended series. Very similar results were obtained with M = 50 year (not shown).

The significant T-EOFs, ordered by decreasing variance captured, along with the associated periods and variances are the following: the pair (1,2) has a period of 3.1 year

and a variance of 18%; the pair (3,4) a period of 2.2 year and a variance of 14%; the pair (5,6) a period of 3.8 year and a variance of 13%; the pair (7,8) a period of 14 year and a variance of 10%; and pair (9,10) has a period of 7.8 year and a variance of 7%. The above periods were also identified as significant at the 95% level using MTM applied to the detrended time series (Table 2), except the 14-year SSA pair (7,8), which was significant in the MTM analysis at the 90% level only. In Fig. 3 we show the MC-SSA and MTM spectra, along with the statistical significance of the peaks.

3.2 The tree-ring record from the Golan Heights

The ring-width records of *Quercus Infectoria* (also called Aleppo oak or Cyprus oak) from the Golan Heights extend over 210 years, 1757–1967; see Fig. 2b. This data set is part of an extensive dendrochronological survey carried out in the Golan Heights in 1967 by Yehuda Feliks (the father of this paper's lead author); see Feliks (1968).

SSA was applied to tree-ring records first by Cook et al. (1995). For our record, the nonlinear trend is captured by the first two eigenmodes of the SSA analysis with a 40-year window. The detrended series was analyzed by MC-SSA with the same window width; very similar results were obtained with M = 50 year. The significant pairs are: pair (1,2) with a period of 25 year and 37% of the variance; pair (3,4) with a period of 14 year and 20% of the variance; pair (6,7) with a period of 10 year and 12% of the variance; and pair (9,10) with a period of 7.7 year and 6% of the variance. We also applied MTM analysis, with 3 tapers and a spectral resolution of 0.03 cycle/year, to the detrended time series. The above frequencies were all significant at the 99% level.

The significant pairs with dominant periods that are equal to 7.7 years or longer capture 75% of the variance of the detrended series. This raises the possibility that the trees integrate climatic effects over several years: the trees' physiology seems to act like a low-pass filter on the climatic signals and thus enhance the low-frequency oscillations. The oscillatory modes of 14 years and 7.7 years are also prominent in the Jerusalem precipitation records.

3.3 The Nile River records

Kondrashov et al. (2005; KFG hereafter) studied in great detail the high- and low-water records for the Nile River over the 1300-year time span 622 A.D.–1922 A.D. They found periodicities of 2.2, 4.2, 7.2, 12, 19 and 64 year; some of these periodicities had already been found and discussed in the abundant literature focusing on these records, as reviewed by KFG. For instance, the 2.2- and 4.2-year signals had been attributed to the long-established connection between the Nile River discharge and the ENSO phenomenon in the Indo-Pacific Ocean (Ropelewski and Halpert, 1987, 1989; Quinn, 1992; Camberlin, 1995; Wang and Eltahir, 1998).

KFG's novel and striking result was the clear presence of a 7.2-year signal in the high-water record. A 7–8-year peak has been well documented in several oceanic and atmospheric fields extending over the North Atlantic basin (Moron et al., 1998; Wunsch, 1998; Da Costa and Colin de Verdière, 2002; Dijkstra and Ghil, 2005; Simonnet et al., 2005). Hence, KFG hypothesized that the 7.2-year mode in the Nile River records demonstrates the extent of the North Atlantic influences, all the way into East Africa's tropical regions. The research reported in the present paper was largely motivated by the need to examine more closely this hypothesis.

The high-water record corresponds to the maximum height of Nile floods, a height that is reached in August–September, when more than 85% of the flow in the Nile River is supplied by the Blue Nile and Atbara River, whose sources lie on the Ethiopian Plateau. This plateau reaches altitudes above 2200 m, and the summer monsoonal rainfall over it peaks between June and September (Wang and Eltahir, 1998; Block and Rajagopalan, 2007). Thus, although the Nile's high water stand was measured by the nilometer at Rhoda Island near Cairo, it is a proxy for rainfall over the Ethiopian Plateau. The measurements at Rhoda Island ceased in 1922, because of the Lower, or Older, Aswan Dam, built at the beginning of the 20th century to regulate the Nile River flow.

To extend the records studied by KFG, we used existing measurements of the monthly volume flow for the century 1869–1969 at Aswan, provided in the hydrographic data sets of the National Center for Atmospheric Research (NCAR); see http://dss.ucar.edu/cgi-bin/rdabrowse?nb=true&c=topic&cv=Hydrosphere. There is a strong correlation between the summer (July–September) volume flow and the high level of the Nile River near Cairo, since 90% of the annual flow is during the summer and most of it is due to the Blue Nile. Thus we can extend the high-water records of the Nile River by using the volume flow for the years after 1922, and up to 1969, when the new, higher Aswan Dam was built.

The extension of the KFG high-water record to the more recent past is done by linear regression

$$h = a\nu + b, \tag{6}$$

where h is the dependent variable, namely the high-water stand near Cairo, while the independent variable v is the yearly mean volume flow near Aswan. The regression

parameters, a = 1.66 and b = –0.83, were found from the overlapping time interval of $h(t)$ and $v(t)$ during the years 1869–1922. During this interval, the correlation between the time series of h and v is 0.93. In Fig. 4a, the observed high-water record and the one estimated according to Eq. (6) are shown for the interval of overlap. The estimated values are clearly quite accurate, and so the high-water record of the Nile at Cairo, extended until 1969, is shown in Fig. 2a. The spectral characteristics of this record (not shown) are quite similar to those in KFG, with the differences clearly attributable to this record's relative shortness and to climatic changes between the earlier centuries and 1869–1969.

3.4 North Atlantic Oscillation (NAO)

The NAO has been studied extensively over the last two decades (Hurrell et al., 2003), and its strength has been quantified using several indices. We use here the monthly index over the years 1823–2000, as compiled by Jones et al. (1997); see Fig. 2d. This index is the difference between the normalized sea level pressure at Gibraltar and the normalized sea level pressure over southwestern Iceland. Jones and colleagues used early instrumental data back to 1823. The data set has been modified in November 2000 and the effect of this change is most evident in the summer; see http://www.cru.uea.ac.uk/~timo/projpages/nao_update.htm.

Here we revisit the index using a somewhat different approach, i.e., we apply M-SSA with 12 channels, each channel being the NAO index in a given month of the year: channel 1 is the index for January, channel 2 for February, and so on, while the time step is 1 year. The window width is again M = 40 year.

The significant oscillatory modes for this M-SSA analysis have periods of 7.7, 5.5, 4, 3.2 and 2.2 years. Each of these periods is dominant for a subset, or group, of

calendar months. The most prominent oscillatory mode has the period of 7.7 year that is familiar from KFG and it appears as the leading reconstructed component, RC[1,2]. This mode is prominent during the winter months of December, January and February (DJF), but also in August and October. In the other calendar months, the amplitude of this mode is smaller at least by a factor of three. Rogers (1984), Robertson (2001), Gámiz-Fortis et al. (2002) and Paluˇs and Novotná (2004) also found an oscillation with a period of about 7.7 year in the NAO index. A quasi-biennial component is present in the closely related Arctic Oscillation, constructed from hemispheric sea level pressures, as well (Trenberth and Paolino, 1981; Robertson, 2001). We applied also MTM analysis, with 3 tapers and a spectral resolution of 0.03 cycle/year, to the winter time series (December–March) and in August. The above frequencies were all significant at the 95% level.

Below we concentrate mainly on two seasons. For boreal winter, i.e. December–March, we use the average index value for these four months, while in summer we use the index value for August.

The main significant oscillatory modes of the above climatic time series are summarized in Table 2. The oscillatory modes appearing in the table are found to be significant at the 95% level against a null hypothesis of red noise, in both SSA and MTM.

4. Synchronized modes

Oscillatory modes with periods around 4, 7–8 and 14 years are thus present in the records from the North Atlantic, Eastern Mediterranean, and Ethiopian Plateau (Table 2). This clustering raises the possibility of teleconnections between the climate variations in these regions. We next examine separately the synchronization of each periodicity between

regions to help determine the source region of the oscillatory mode and its role in the dynamics of each region.

The method of synchronization analysis was described in section 2. The analysis is applied to the overlapping portion of the two RC time series in question, with each series normalized by its variance in the overlapping part. In the following, we chose the window width M in the M-SSA to be about $N'/3$, where N' is the length of the overlapping portion of the two time series in question.

4.1 Nile River floods and the NAO

The overlapping time interval of the extended high-water Nile records and the NAO index is 1825–1971. Monsoon rains over the Ethiopian Plateau occur during the boreal summer, along with the northward seasonal migration of the intertropical convergence zone (ITCZ), and hence we examine here the summer index of the NAO. The 7.7-year oscillation is prominent in the NAO index during the boreal summer only in August.

We apply two-channel SSA where channel 1 consists of the high-water Nile records and channel 2 of the NAO index for August. The analyses carried out with a window width of M = 30 and 40 years gave almost identical results. The significant oscillatory components have periods of 7.6, 4.3, 3.3 and 2 years.

To concentrate on the interannual periodicities, we first removed the trend, as captured by $RC^{(1,2)}$ of the M-SSA analysis with a 35-year window. We then applied M-SSA again to the detrended time series with M = 35 year. The MC-SSA spectrum is shown in Fig. 4b, along with the statistical significance. The resulting leading oscillatory mode $RC^{(1,2)}$ has a period of 4.3 years, and accounts for 17% of the variance of the detrended series (see Fig. 5b).

The mean phase difference, cf. Eq. (2b), is 3.11 radian = 2.1 year, and the standard deviation, cf. Eq. (4a), is σ = 0.11 radian = 0.96 month. The amplitude correlation, cf. Eq. (4b), is 0.92, and so the synchronization is complete, i.e. of (FPA) type, with a near phase opposition between the NAO index and Nile flow (see Fig. 5b). The energy ratio $E(\mathrm{RC}x_1)/E(\mathrm{RC}x_2)$ is ε = 0.97, where x_1 corresponds to the Nile record and x_2 to the NAO index. This ratio is quite close to unity, suggesting that the coupling between the climate systems that trigger the 4.3-year oscillation in the two regions is very strong. Since the energy ratio is about 1, we cannot identify the direction of influence, but physical plausibility clearly tilts towards the NAO being causal.

The second oscillatory mode is represented by $\mathrm{RC}^{(6,7)}$, has a period of 7.6 year, and captures 13% of the variance (see Fig. 5a). The mean phase difference is of 2.5 year and is discussed below, while the standard deviation is σ = 0.23 radian = 0.28 year. The amplitude correlation is 0.95, so the synchronization is complete, of (FPA) type. The energy ratio is ε = 0.28, suggesting that the coupling is moderate and that the NAO induces the 7.6-year oscillation in the Nile River. A potential teleconnection mechanism between the climate systems in the two regions that triggers this oscillation is discussed below, in connection with Fig. 7.

The oscillatory mode $\mathrm{RC}^{(9.10)}$ has a period of 3.3 year and accounts for 10% of the variance (Fig. 5c). The mean phase difference is 1.37 radian = 0.72 year (discussed below) and the standard deviation is σ = 0.42 radian = 0.22 year. The amplitude correlation is 0.85, so the synchronization is almost complete. However, the ratio $E(\mathrm{RC}x_1)/E(\mathrm{RC}x_2)$ = 0.11, suggesting that the coupling is quite weak.

To explore the teleconnection mechanism between the North Atlantic and the Nile River floods, Fig. 6a shows the mean low-level moisture fluxes during the month of August, computed from the National Centers for Environmental Prediction (NCEP)-NCAR atmospheric reanalyses (Kalnay et al., 1996); the pattern is qualitatively similar throughout the summer season (June–September; not shown). From the figure it follows that the rain over the Ethiopian Plateau is largely a result of moisture flux convergence from the south and north, associated with northward displacement of the ITCZ. Northward fluxes during boreal summer advect moisture from the equatorial Atlantic, and possibly the Indian Ocean — see also Rodwell and Hoskins (1996) and Raicich et al. (2003) — while the southward flux originates over the eastern Mediterranean.

The Somali jet transports humid air from the western part of the Indian Ocean northwestward, to the eastern slopes of the Ethiopian Plateau, which reach altitudes above 2000 m; this humidity flux is plotted as track 1 in Fig. 6b. As this humid air climbs above the plateau, it cools, condenses and discharges its humidity as rain. Most of the rain from this source, however, falls over the eastern part of the Plateau and so its role in contributing to the flow of the Blue Nile is limited.

The second track of humid air to the Ethiopian Plateau starts off the equatorial Atlantic Ocean and is associated with the West African monsoon; this moisture flux is limited to the shallow layer beneath the African easterly jet at 700 hPa (Nicholson and Grist, 2003), and is plotted as track 2 in Fig. 6b. A significant southward flux of moisture from the Mediterranean and Red Sea is visible in Fig. 6a, with some moisture flux divergence over the Eastern Mediterranean; this humidity contribution is shown as track 3 in Fig. 6b. This third track is also found in maps of humidity flux drawn by James

(1995, p. 250), Mariotti et al. (2002), and Mohamed et al. (2005). As these air masses reach the northern slopes of the Ethiopian Plateau, they ascend to levels above 3000 m, near the core of the African easterly jet. At these altitudes, the jet transports the ascending air over the Plateau, where it is cooled, condensed and discharges its moisture as rain in the catchment area of the Blue Nile and the Atbara River.

Although most studies on the NAO have focused on the winter season, Folland et al. (2009) have recently studied its summertime expression during July and August. They demonstrate that the NAO's positive phase is associated with anomalously wet conditions over the western Mediterranean, and anomalously dry conditions across the Sahel; see also Hurrell and Folland (2002). Correlation maps between the NAO index and the low-level moisture flux vector (not shown) indicate a broad-scale influence of the NAO on the low-level flow over North Africa and the Mediterranean; in its positive phase, the summertime NAO tends to weaken the West African monsoon (described as track 2 above), while tending also to strengthen the flow across the Mediterranean and Egypt associated with track 3.

A mean phase difference of 2.5 year in the 7.6-year oscillation and 2.1 year in the 4.2-year oscillation is found in the coupled oscillatory modes of the NAO index and the Nile records. The almost exact phase opposition at the 4.2-year period indicates that the negative phase of the NAO is associated with enhanced Nile River flow at this period, with the West African monsoon (track 2) most active. For the 7.6-year period, the delay in the Nile River flow is closer to a quarter period than to a half-period, and it is thus more likely that the Eastern Mediterranean track 3 plays a greater role at this period.

4.2 The rain in Jerusalem and the NAO

The 134-year time interval of overlap between the precipitation records in Jerusalem and the NAO index is 1861–1993. Since the rainy season in the eastern part of the Eastern Mediterranean is during the winter months, we use the mean value of the NAO index during December–April in our analysis.

We apply M-SSA with channel 1 consisting of the NAO index and channel 2 being the precipitation record in Jerusalem. The analyses carried out with M = 30 and 40 year gave almost the same results for both values of M. The significant oscillations have periods of 7.8, 3.8, 3.1 and 2 years.

To better study the interannual periodicities we first removed the trend, captured by $\mathrm{RC}^{(1)}$ of the M-SSA analysis with a 35-year window. We then applied M-SSA to the detrended time series with M = 35 years. The MC-SSA spectrum, along with the statistical significance, is shown in Fig. 7a.

The leading oscillatory mode, $\mathrm{RC}^{(1,2)}$, has a period of 7.8 years, and accounts for 19% of the variance (Fig. 7b). The mean phase difference is – 0.17 radian = – 0.2 year, with a standard deviation of σ = 0.05 radian = 0.06 year. The amplitude correlation is 0.96, and so the synchronization is of (FPA) type. The energy ratio ε in this mode is $E(\mathrm{RC}x_1)/E(\mathrm{RC}x_2) = 2.8$, where x_1 corresponds to the NAO index and x_2 to the Jerusalem rainfall, suggesting that it is the NAO that induces the 7.8-year oscillation in Jerusalem rainfall and that the coupling is moderate.

The in-phase relationship between the NAO index and Jerusalem rainfall is consistent with the results of Dünkeloh and Jacobeit (2003). In the positive phase of the NAO, higher pressures extend broadly over southern Europe and the Mediterranean, but

over the far Eastern Mediterranean surface pressures are lower, with an upper-level trough extending all the way from Iceland. This trough pushes very cold air over the relatively warm Mediterranean Sea, and results in unstable air that leads to increased rainfall over the eastern and southeastern rim of the basin.

On the other hand, Eshel and Farrell (2000) claim the opposite for the eastern and southern parts of the Eastern Mediterranean. They found that the correlation between the NAO index and the average precipitation in the whole Eastern Mediterranean is negative. Their conclusion is based on averaging precipitation from the region, but in fact the stations in western Turkey, which are the densest, determine their average precipitation values. Thus the results of Eshel and Farrell (2000) are relevant only to the rainfall in western Turkey, and not to the eastern and southern part of the Eastern Mediterranean, where the effect has the opposite sign.

The oscillatory mode $RC^{(5,6)}$ has a period of 3.1 year, and accounts for 12% of the variance. The mean phase difference is 18.7 radian = 9.2 year, with a standard deviation of σ = 10.6 radian = 5.2 year. The amplitude correlation is 0.29, and so the Eastern Mediterranean and the NAO are not synchronized at this period.

The oscillatory mode $RC^{(7,8)}$ has a period of 3.8 year, and accounts for 11% of the variance (Fig. 7c). The mean phase difference is – 0.27 radian = 0.13 year, and the standard deviation, σ = 0.19 radian = 0.11 year. The amplitude correlation is 0.84, and so the synchronization type is close to (FPA). The energy ratio ε_{78} is $E(\mathrm{RC}x_1)/E(\mathrm{RC}x_2)$ = 0.8, thus suggesting that the coupling is strong. Since the ratio is close to unity, it does not determine the direction of influence, but physical reasoning again leads us to suspect that it is the NAO that induces this oscillation in the Eastern Mediterranean.

4.3 Tree rings and Jerusalem precipitation

The 107-year time interval of overlap between the tree-ring record in the Golan Heights and Jerusalem precipitation extends over 1861–1968. We applied M-SSA to this time interval, with channel 1 consisting of the tree-ring widths and channel 2 of Jerusalem precipitation. The analysis was carried out with M = 30 and 40 years, with very similar results in both cases. The significant oscillations have periods of 12.5, 7.8, and 3.8 years.

To better study the interannual periodicities, we first removed the trend, captured by $\mathrm{RC}^{(1-4)}$ with M = 30 years. We then applied M-SSA to the detrended time series with the same window width.

The oscillatory mode $\mathrm{RC}^{(1,2)}$ has a period of 3.8 years, and accounts for 17% of the variance. The mean phase difference is 0.8 radian = 0.48 year, with standard deviation σ = 1.23 radian = 0.7 year. The amplitude correlation is 0.77, and so the synchronization type is (FP). The energy ratio ε_{12} is $E(\mathrm{RC}x_1)/E(\mathrm{RC}x_2) = 0.01$, where x_1 corresponds to the tree-ring records and x_2 to the Jerusalem precipitation records. This ratio suggests that — while the coupling is quite weak — the rainfall induces the 3.8-year oscillation in the tree growth, in agreement with intuition.

The oscillatory mode $\mathrm{RC}^{(3,4)}$ has a period of 12.5 years, and contains 16% of the variance; it is shown in Fig. 8. The mean phase difference is 1.57 radian = 3.3 year and its standard deviation is σ = 1.64 radian = 3.26 year, while the amplitude correlation is 0.98. It is surprising that the amplitude correlation is so high, although the phase is not synchronized; we thus appear to have a synchronization type that was not previously encountered, but can be labeled (FA). The energy ratio is $E(\mathrm{RC}x_1)/E(\mathrm{RC}x_2) = 0.70$; it

shows that the coupling is strong and suggests it is the rainfall that induces the 12.5-year oscillation in the tree growth, as expected.

The oscillatory mode $RC^{(11,12)}$ has a period of 7.8-year, and captures 10% of the variance. The mean phase difference is 0.42 radian = 0.5 year, and its standard deviation is σ = 2.47 radian = 3.07 year; the amplitude correlation is –0.54, and so the synchronization type is (F). The ratio ε_{34} is $E(RCx_1)/E(RCx_2) = 0.41$, suggesting that the coupling is moderate and that the rainfall induces the 7.8-year oscillation in the tree-ring record as well.

It might appear somewhat surprising that the rainfall record in Jerusalem and the tree-ring record in the Golan Heights exhibit such a relatively weak degree of synchronization. Two main climatic factors determine tree growth: the amount of rain and the temperature. Usually more rain causes larger tree-ring growth, while cool winters result in less growth. Since the rainy winters are also cooler in the Eastern Mediterranean, these two factors have an opposing effect on the tree growth, thus tending to weaken the rainfall signal in the tree-ring record.

5. Concluding remarks

5.1 Summary

Evidence for oscillatory modes of variability over the North Atlantic, Ethiopian Plateau and Eastern Mediterranean was examined using climate records from each region: the NAO index for the North Atlantic and Nile River high-water records for the Ethiopian Plateau, while the climate proxies for the Eastern Mediterranean were precipitation in Jerusalem and a tree-ring record from the Golan Heights.

Statistically significant oscillatory modes — having periods of about 4 and 7–8 years — were identified in all records. Such a clustering of periodicities raises the possibility of teleconnections between these regions (Ghil et al., 2002a). Other significant oscillatory modes were found in some of the records only; in particular, a 14-year mode is present in Jerusalem rainfall and tree rings.

We have approached climatic teleconnections between regions in terms of synchronization of chaotic oscillators. Our approach is based, on the one hand, on the work of J. Kurths and colleagues (Rosenblum et al., 1996; Boccaletti et al., 2002; Pikovsky et al., 2003; Osipov et al., 2003) and, on the other, on pre-filtering and spectral analysis of the time series of interest, via singular-spectrum analysis (SSA) and multi-channel SSA (M-SSA). In addition, we examined the strength of the coupling and the direction of influence by examining the energy (or variance) ratio between various channels, in separate frequency bands identified by the M-SSA.

The methodology was presented in section 2, and illustrated by its application to the coupled Rössler oscillators previously used by Rosenblum (1996). As the coupling between the oscillators increases, their time series synchronize, first in frequency (F), then in phase (FP), and finally in amplitude as well (FPA). In addition to following these steps in the synchronization, as defined by Osipov et al. (2003), we studied the route to synchronization by examining the joint spectra of the oscillatory modes, using two-channel M-SSA.

For the two coupled Rössler oscillators, the strength of the coupling can be measured, without explicit reference to the value of the coupling constant C in Eqs. (5), by examining the ratio $\varepsilon_{k,k+1}$ of the energy (or variance) in the two channels of the

reconstructed components (RCs) of the oscillatory mode (k, k + 1) under study. As the coupling between the two oscillators increases, the energy ratio tends to unity and the energy accumulates in a single oscillatory mode.

We applied the above method to examine the synchronization between our climatic time series, based on the broad theoretical concept that the climate system can be described as a large, or even infinite, number of coupled oscillators, as discussed at the end of section 2; see also Ghil and Childress (1987) and Lorenz (1991, 1996). Our hypothesis is that the commonality between several oscillatory modes found in the set of climate indices analyzed is due to the coupling between the oscillators. The significant oscillatory modes in the joint spectra of the climate records studied here, their synchronization type, and the energy ratio in each mode are summarized in Table 3.

The 7–8-year oscillatory mode in all three regions and four types of records is completely synchronized, i.e. of (FPA) type, and the energy-ratio analysis suggests that the NAO induces this mode in the other regions. We discuss the possible origin of this mode in the North Atlantic further below. The boreal-summer teleconnection between the NAO and the Ethiopian Plateau's rainfall, as captured by the Nile River's high-water record, is likely to involve the NAO's influence on the West African monsoon (Folland et al., 2009).

An (FPA)-type synchronization at 7.8 year is also found between the North Atlantic and the eastern part of the Eastern Mediterranean during winter, which is the rainy season in the latter region. This teleconnection can be explained using the results of Dünkeloh and Jacobeit (2003), who showed that, during the winter, a low-pressure anomaly extends from Northern Europe to the southern and eastern part of the Eastern

Mediterranean. The NAO index determines the strength of this low-pressure anomaly and, therewith, the amount of rain in the eastern and southern part of the Eastern Mediterranean.

The 7–8-year mode was found to be prominent in all our indices during December–February, August and October. It might be induced by an oscillation of similar period in the position and strength of the Gulf Stream's sea surface temperature (SST) front in the North Atlantic. This oscillation in SSTs and sea level pressures over the entire basin was identified in many previous studies (Deser and Blackman, 1993; Moron et al., 1998; Joyce et al., 2000; Da Costa and Colin de Verdière, 2002), while Wang et al. (2004) showed that it is the Gulf Stream region alone that affects the NAO. The 7–8-year variability in the Gulf Stream, in turn, has been attributed to an oscillatory gyre mode of the North Atlantic's wind-driven circulation (Jiang et al., 1995b; Ghil et al., 2002b; Dijkstra and Ghil, 2005; Simonnet et al., 2005; Sushama et al., 2007).

Finally, Feliks et al. (2004, 2007) demonstrated in a simplified atmospheric the impact of a narrow and vigorous SST front, like the Gulf Stream front, on the atmosphere above it and downstream. Minobe et al. (2008) confirmed the predictions of Feliks et al. (2004, 2007) by carrying out calculations along these lines in a high-resolution, coupled general circulation model, with realistic SST forcing, and compared the model results with satellite observations.

An oscillatory mode with a period of about 4 years is found in all our climate records as well. A teleconnection to the Ethiopian Plateau, related to the quasi-quadrennial (or low-frequency) ENSO mode (Rasmusson et al., 1991; Jiang et al., 1995a) has been the subject of several studies (e.g., Giannini et al., 2005; Chiang and Sobel,

2002; Lintner and Chiang, 2007); it appears to be associated with ENSO influence on changes in tropospheric static stability across the tropical atmosphere that affect convection over Ethiopia. There is no evidence, though, that this mode that is shared by the NAO and the Eastern Mediterranean is induced by ENSO. Additional analyses not reported here show that the energy ratio in the joint M-SSA spectra of the NAO index and of the Southern Oscillation Index is very small, $\varepsilon = 0.1$.

On the other hand, the energy ratio in the two-channel, 4-year M-SSA mode for the NAO index and Jerusalem rainfall is $\varepsilon = 0.8$. We suggest that this mode may be induced in the North Atlantic climate by a 4-year oscillation (possibly a harmonic of the 7–8-year oscillation; see Moron et al., 1998) of the position of the Gulf Stream SST front. In the joint spectra of the Nile River record and the NAO index, a 4.2-year oscillatory mode is also prominent. The synchronization type of this mode is (FPA), and the coupling between the two regions is very strong, with an energy ratio of $\varepsilon = 0.97$. Thus the Ethiopian Plateau appears to exhibit independent teleconnections, at a period of about 4 years, with both the North Atlantic and ENSO.

In the Eastern Mediterranean, an oscillatory mode with a period of about 12–14 years is prominent in the Jerusalem rainfall record and in tree rings from the Golan Heights. The oscillatory mode of the joint spectral analysis for the rainfall and tree rings has a period of 12.5 years. Although the coupling between the rainfall record and the tree rings is relatively strong, the synchronization type is of (FA) type. This type is differs from the three types introduced by Osipov et al. (2003) — which were also the ones we found useful in other two-channel M-SSA analyses here — series since the amplitudes are well correlated, while the phases are not synchronized.

We attribute this unusual result to the physiology of tree-ring growth. Two principal climatic factors determine this growth, namely rainfall and temperature. In the Eastern Mediterranean, rainy winters are also cooler so these two factors have a tendency to cancel out. In the tree-ring record, the significant periods that are longer than 7 years capture 75% of the variance of the detrended time series. This raises the possibility that the trees' physiology acts like low-pass filter on the climatic signals.

5.2 Discussion

This work grew out of Kondrashov et al. (2005; KFG in the main text) finding a 7–8-year oscillation in a 1300-year long record of Nile River water levels. Searching for the sources of the Nile has been a multi-millennial quest that started with up-river military expeditions of the pharaohs, to find and protect the headwaters of the Nile. The quest continued with the one for the mythical Prester John in the Middle Ages, and only ended in the 19th century, with the European expeditions that finally reached the sources of the White and Blue Nile. Likewise, the search for the explanation of Joseph's dream about the alternation of seven fat and seven lean years goes back several thousand years and might not be over yet.

We suppose that increasing the number of coupled oscillators in a system like that of section 2.2 here — as in the work of Brunnet et al. (1994) and of Lorenz (1991, 1996) — will make the synchronization problem much richer: the number of synchronized modes will increase, probably in rough proportion to the number of oscillators. The route to synchronization might still be similar, however: as the coupling between the oscillators increases, more energy will accumulate in the RCs of the oscillatory modes associated with lower frequencies and possibly broader spatial patterns. The whole system will

synchronize when most of the energy accumulates in the RC mode obtained by projection onto the lowest pair of ST-EOFs, and the significant eigenvalues will all merge into one value. A model of this type might explain the prevalence of a small number of oscillatory patterns in the global climate system.

The evidence presented here for oscillatory climate modes with planetary-scale teleconnections may have implications for prediction, especially at lead times beyond seasonal ones, for which dynamical models are not yet useful. Robertson et al. (2001) demonstrated river-flow predictability up to 4 years in advance for low-flow years on the Paraná River in southeastern South America. The predictions were based on an 8-year periodicity in the river flow's time series, as identified by SSA. Robertson and Mechoso (1998) found this periodicity to be related to SST anomalies in the tropical North Atlantic. Further work is required to relate these findings to those of the present paper.

APPENDIX A. M-SSA and synchronization

The purpose of this appendix is to show that the results for the coupled Rössler oscillators in section 2.2 are not an artifact of the M-SSA analysis. To do so, we illustrate the performance of our methods on two even simpler synthetic-data examples.

First, we apply our synchronization analysis to two phase- and amplitude-modulated, noise-perturbed sine curves:

$$f_1(t)=A(1+\omega_1)\sin[t+\cos(\pi t+\omega_1)]+\omega_1 \quad , \qquad (7a,b)$$

$$f_2(t) = A(1+\omega_2)\sin\left[t\alpha + \cos\left(\sqrt{2}t + \omega_2\right)\right] + \omega_2.$$

Here $A = 1$, while ω_1 and ω_1 are white noises that are normally distributed, with mean zero and variance 1. In the first example (Figs. 9a, b) we set $\alpha = 1$ so that f_1 and f_2 have

the same underlying period, but have different (noisy) phase modulations; the underlying periodicities will thus be synchronized, at least in frequency. The cross-spectra of f_1 and f_2 were computed by applying two-channel SSA, with a window width of $M = 100\Delta t = 10$ time units.

The RC associated with the first ST-EOF pair, $\mathrm{RC}^{(1,2)}$ is shown in Fig. 9b; it captures 16% of the variance. This pair is completely synchronized (σ=0.05 radians) according to the phase-difference criteria of Osipov et al. (2003), with an energy ratio of $E(\mathrm{RC}x_1)/E(\mathrm{RC}x_2) = 1.01$. In the second example (Fig. 9c,d) we set α=1.3 so that the periods are different and the underlying periodic signals are not synchronized. The two time series are shown in Fig. 9c; note that f_1 is the same in both examples, and is visualized by the dashed curves in Figs. 9a and 9c. The RC associated with the first ST-EOF pair, $\mathrm{RC}^{(1,2)}$ is shown in Fig. 9d and captures 9% of the variance. This pair is not synchronized, since the phase-difference variance is σ=17.5 radians, while the energy ratio $E(\mathrm{RC}x_1)/E(\mathrm{RC}x_2) = 0.58$.

These two examples illustrate the application of the analysis to noisy time series with known underlying periodicities and differing synchronization characteristics. It clearly shows that the method works when it should and doesn't when it shouldn't.

Acknowledgements. It is a pleasure to thank D. Yakir for the precipitation records from Jerusalem, A. Zukerman for digitizing the tree rings graphs, and many colleagues for useful discussions. Among the latter, G. Duane, A. Groth, J. Kurths and J. J. Tribbia played a significant role in familiarizing us with the literature on synchronization of chaotic oscillators. We thank two anonymous reviewers for insightful and constructive

comments. This work was supported by U.S. Department of Energy grants DE-FG02-07ER64429 and DE-FG02-07ER64439 from its Climate Modeling Programs, and by the European Commission's No. 12975 (NEST) project "Extreme Events: Causes and Consequences (E2-C2)."

References

Allen, M. R., and A. W. Robertson, 1996: Distinguishing modulated oscillations from colored noise in multivariate datasets. *Climate Dyn.,* **12**: 775–784.

Allen, M. R., and L. A. Smith, 1996: Monte Carlo SSA: Detecting irregular oscillations in the presence of coloured noise, *J. Clim.*, **9**, 3373–3404.

Barnston A. G., and R. E. Livezey, 1987: Classification, seasonality and persistence of low-frequency atmospheric circulation patterns. *Mon. Wea. Rev*, **115**, 1083–1126.

Bedrosian, E., 1963: A product theorem for Hilbert transforms, *Proc. IEEE*, **51**, 868–869.

Block, P., and B. Rajagopalan, 2007: Interannual variability and ensemble forecast of upper Blue Nile basin seasonal precipitation. *J. Hydrometeor.*, **8,** 327–343.

Boccaletti, S., J. Kurths, G. Osipov, D.L. Valladares, C.-S. Zhou, 2002: The synchronization of chaotic systems, *Phys. Reports*, **366**, 1–101.

Broomhead, D. S., and G. P. King, 1986: On the qualitative analysis of experimental dynamical systems, in *Nonlinear Phenomena and Chaos*, edited by S. Sarkar, pp. 113–144, Adam Hilger, Bristol, England.

Brunnet, L., H. Chaté and P. Manneville, 1994: Long-range order with local chaos in lattices of diffusively coupled ODEs, Physica D, 78(3-4), 141–154.

Camberlin, P., 1995: June–September rainfall in north-eastern Africa and atmospheric signals over the tropics: A zonal perspective. *Int. J. Climatol.,* **15,** 773–783.

Carton, J. A. and B. S. Giese, 2008: A reanalysis of ocean climate using Simple Ocean Data Assimilation (SODA). *Mon. Wea. Rev.*, **136**, 2999–3017.

Chao, Y., M. Ghil, and J. C. McWilliams, 2000: Pacific interdecadal variability in this century's sea surface temperatures, *Geophys. Res. Lett.*, **27**, 2261–2264.

Chiang, J. C. H., and A. H. Sobel, 2002: Tropical tropospheric temperature variations caused by ENSO and their influence on the remote tropical climate. *J. Climate*, **15**, 2616–2631.

Chiang, J. C. H., and D. Vimont, 2004: Analogous Pacific and Atlantic meridional modes of tropical atmosphere-ocean variability. *J. Climate*, **17**, 4143–4158.

Cook, E. R., B. M. Buckley, and R. D. D'Arrigo, Interdecadal temperature oscillations in the Southern Hemisphere, 1995: Evidence from Tasmanian tree rings since 300 B. C., in *Natural Climate Variability on Decade-to-Century Time-Scales*, edited by D. G. Martinson *et al*., pp. 523–532, National Academies Press, Washington, D. C.

Da Costa, E. D., and A. Colin de Verdière, 2002: The 7.7-year North Atlantic oscillation, *Q. J. R. Meteorol. Soc*., **128A**, 797–817.

Deser, C., and M. L. Blackman, 1993: Surface climate variation over the North Atlantic Ocean during winter: 1900–1999, *J. Clim.,* **6**, 1743–1753.

Dettinger, M. D., M. Ghil and C. L. Keppenne, 1995: Interannual and interdecadal variability in United States surface-air temperatures, 1910–87, *Climatic Change*, **31**, 35–66.

Dijkstra, H.A., and M. Ghil, 2005: Low-frequency variability of the large-scale ocean circulation: A dynamical systems approach, *Rev. Geophys*., RG3002, doi:10.1029/2002RG000122.

Duane, G.S., 1997: Synchronized chaos in extended systems and meteorological teleconnections, *Phys. Rev. E*, **56**, 6475–6493.

Duane, G.S., and J.J. Tribbia, 2004: Weak Atlantic–Pacific teleconnections as synchronized chaos, *J. Atmos. Sci*., **61**, 2149–2168.

Dünkeloh, A., and J. Jacobeit, 2003: CIirculation dynamics of MEDITERRANEAN precipitation variability 1948–98. *Int. J. Climatol.* **23**: 1843–1866

Eshel, G., and B. F. Farrel, 2000: Mechanisms of eastern Mediterranean rainfall variability. *J. Atmos. Sci*., **57**, 3219–3232.

Feliks, Y., 1968: Tree and forest in the Golan Heights. *Teva Vaeretz*, 3–16 (in Hebrew).

Feliks, Y., M. Ghil and E. Simonnet, 2004: Low-frequency variability in the midlatitude atmosphere induced by an oceanic thermal front. *J. Atmos. Sci.,* **61,** 961–981.

Feliks, Y., M. Ghil, and E. Simonnet, 2007: Low-frequency variability in the mid-latitude baroclinic atmosphere induced by an oceanic thermal front, *J. Atmos. Sci*., **64**, 97–116.

Folland, C. K., J. Knight, H. W. Linderholm, D. Fereday, S. Ineson, and J. W. Hurrell, 2009: The Summer North Atlantic Oscillation: past, present and future**.** *J. Climate*, **22**, 1082–1103.

Gabor, D., 1946: Theory of communication. *J. I. E. E.* (London), **93**, 429–457.

Gámiz-Fortis, S. R., D. Pozo-Vázques, M.J. Esteban-Parra, and Y. Castro-Díez: Spectral characteristics and predictability of the NAO assessed through singular spectral analysis, *J. Geophys. Res*., **107**(D23), 4685, 2002.

Ghil, M., and Childress S., 1987: *Topics in Geophysical Fluid Dynamics: Atmospheric Dynamics, Dynamo Theory and Climate Dynamics*, Springer-Verlag, New

York/Berlin/London/Paris/ Tokyo, 485 pp.

Ghil, M., and A. W. Robertson, 2000: Solving problems with GCMs: General circulation models and their role in the climate modeling hierarchy. *General Circulation Model Development: Past, Present and Future,* D. Randall (Ed.), Academic Press, San Diego, pp. 285–325.

Ghil, M., and R. Vautard, 1991: Interdecadal oscillations and the warming trend in global temperature time series, *Nature*, **350**, 324–327.

Ghil, M., M. R. Allen, M. D. Dettinger, K. Ide, D. Kondrashov, M. E. Mann, A. W. Robertson, A. Saunders, Y. Tian, F. Varadi, and P. Yiou, 2002a: Advanced spectral methods for climatic time series*, Rev. Geophys*., **40**(1), pp. **3**.1–**3**.41, doi: 10.1029/2000RG000092.

Ghil, M., Y. Feliks, and L. Sushama, 2002b: Baroclinic and barotropic aspects of the wind-driven ocean circulation, *Physica D*, 167, 1–35.

Giannini, A., R. Saravanan, and P. Chang, 2005: Dynamics of the boreal summer African monsoon in the NSIPP1 atmospheric model. *Climate Dyn.,* **25***,* 517–535.

Henrici, P., 1963: *Error Propagation for Difference Methods*, J. Wiley, New York/London, 73 pp.

Hilbert, D., 1953: *Grundzüge einer allgemeinen Theorie der linearen Integralgleichungen*, Chelsea Publ. Co., New York.

Hurrell, J.W., 1995: Decadal trends in the North Atlantic Oscillation: Regional temperatures and precipitation, *Science*, **269**, 676–679.

Hurrell, J.W., and C.K. Folland, 2002: A Change in the Summer Atmospheric Circulation over the North Atlantic. *CLIVAR Exchanges*, Vol. 25, pp. 52-54.

Hurrell, J. W., Y. Kushnir, G. Ottersen, and M. Visbeck, 2003: An overview of the North Atlantic Oscillation. *The North Atlantic Oscillation: Climatic Significance and Environmental Impact, Geophys. Monogr.,* Vol. 134, American Geophysical Union, pp. 1–35.

Isaacson, E., and H. B. Keller, 1966: *Analysis of Numerical Methods*, J. Wiley, New York/London/Sydney, 541 pp.

James, I. N., 1995: *Introduction to Circulating Atmospheres*, Cambridge University Press, Cambridge, 422 pp.

Janjarasjitt, S., and K.A. Loparo, 2008: An approach for characterizing coupling in dynamical systems, *Physica D*, **237**, 2482–2486, doi:10.1016/j.physd.2008.03.003

Jiang, N., J. D. Neelin and M. Ghil, 1995a: Quasi-quadrennial and quasi-biennial variability in the equatorial Pacific. *Clim. Dyn.*, **12**, 101–112.

Jiang, S., F.-F. Jin, and M. Ghil, 1995b: Multiple equilibria, periodic, and aperiodic solutions in a wind-driven, double-gyre, shallow-water model, *J. Phys. Oceanogr.*, **25**, 764–786.

Jones, P.D., T. Jonsson, and D. Wheeler, 1997: Extension to the North Atlantic Oscillation using early instrumental pressure observations from Gibraltar and South-West Iceland. *Int. J. Climatol.* **17**, 1433–1450.

Joyce, M. T., C. Deser and M. A. Spall, 2000: The relation between decadal variability of subtropical mode water and the North Atlantic Oscillation. *J. Climate*, **13**, 2550–2569.

Keppenne, C. L., and M. Ghil, 1993: Adaptive filtering and prediction of noisy multivariate signals: An application to subannual variability in atmospheric angular momentum, *Intl. J. Bifurcation & Chaos*, **3**, 625–634.

Kondrashov, D., Y. Feliks, and M. Ghil, 2005: Oscillatory modes of extended Nile River records (A.D. 622–1922), *Geophys. Res. Lett.*, **32**, L10702, doi:10.1029/2004GL022156.

Lintner, B. R., and J. C. H. Chiang, 2007. Adjustment of the remote tropical climate to El Niño conditions. *J. Climate*, **20**, 2544-2557.

Lorenz, E. N., 1963: Deterministic nonperiodic flow. *J. Atmos. Sci.*, **20**, 130–141.

Lorenz, E.N., 1991: Dimension of weather and climate attractors, *Nature*, **353**, 241–244.

Lorenz, E. N., 1996: Predictability: A problem partly solved. *Proc. Seminar on Predictability,* Vol. 1, Reading, United Kingdom, ECMWF, pp. 1–18.

Maloney, E. D. and J. Shaman, 2008: Intraseasonal variability of the West African monsoon and Atlantic ITCZ. J. Climate, 21, 2898–2918.

Mann, M.E., and J.M. Lees, 1996: Robust estimation of background noise and signal detection in climatic time series, *Clim. Change,* **33**, 409–445.

Mantua, N.J., S. R. Hare, Y. Zhang, J. M. Wallace, and R.C. Francis, 1997: A Pacific interdecadal climate oscillation with impacts on salmon production, *Bull. Amer. Meteorol. Soc.*, **78**, 1069–1079.

Maraun, D., and J. Kurths, 2004: Cross wavelet analysis: significance testing and pitfalls, *Nonlin. Processes Geophys.*, **11**, 505–514.

Mariotti, A., M. V. Struglia, N. Zeng and K.-M. Lau, 2002: The hydrological cycle in the Mediterranean region and implications for water budget on the Mediterranean Sea. *J. Climate*, **15**,16741690.

Marple, Jr., L., 1999: Computing the discrete-time analytic signal via FFT, *IEEE Trans. Acoustics Speech Signal Processing*, **47**, 2600–2603.

Minobe, S., A. Kuwano-Yoshida, N. Komori, S.-P. Xie, and R.J. Small, 2008: Influence of the Gulf Stream on the troposphere. *Nature*, **452**, doi:10.1038/nature06690.

Mohamed, Y. A., B. J. J. van den Hurk, H. H. G. Savenije and W. G. M. Bastiaanssen, 2005: Hydroclimatology of the Nile: Results from a regional climate model. *Hydrol. Earth System Sci*., **9**, 263278.

Moron, V., R. Vautard, and M. Ghil, 1998: Trends, interdecadal and interannual oscillations in global sea-surface temperatures, *Clim. Dyn.*, **14**, 545–569.

Nicholson, S. E., and J. P. Grist, 2003: The seasonal evolution of the atmospheric circulation over West Africa and Equatorial Africa. *J. Climate*, **16**, 1013–1030.

Osipov, G.V., B. Hu, C. Zhou, M.V. Ivanchenko, and J. Kurths, 2003: Three types of transitions to phase synchronization in coupled chaotic oscillators, *Phys. Rev. Lett.*, **91**, doi: 10.1103/PhysRevLett.91.024101.

Paluˇs, M. and D. Novotná, 2004: Enhanced Monte Carlo Singular System Analysis and detection of period 7.8 years oscillatory modes in the monthly NAO index and temperature records, *Nonlin. Processes Geophys*., **11**, 721–729.

Paluˇs, M. and D. Novotná, 2006: Quasi-biennial oscillations extracted from the monthly NAO index and temperature records are phase-synchronized. *Nonlin. Processes Geophys*., **13**, 287–296.

Panter, P., 1965: *Modulation, Noise, and Spectral Analysis*. McGraw-Hill, New York.

Philander, S. G. H., 1990: *El Niño, La Niña, and the Southern Oscillation*, Academic Press, San Diego, 293 pp.

Pikovsky, A., M. Rosenblum and J. Kurths, 2003: *Synchronization–A Universal Concept in Nonlinear Sciences*, Cambridge University Press.

Plaut, G., and R. Vautard, 1994: Spells of low-frequency oscillations and weather regimes in the Northern Hemisphere. *J. Atmos. Sci.,* **51,** 210–236.

Pozo-Vázques, D., Esteban-Parra, M. J., Rodrigo, F. S., and Castro-Díez, Y. , 2001: A study of NAO variability and its possible nonlinear influence on European surface temperature, *Clim. Dyn*., 17, 701–715.

Raicich, F., N. Pinardi and A. Navarra, 2003: Teleconnections between Indian monsoon and Sahel rainfall and the Mediterranean, *Intl. J. Climatol*., **23**, 173–186.

Rasmusson, E.M., and T.H. Carpenter, 1982: Variations in tropical sea surface temperature and surface wind fields associated with the Southern Oscillation/El Niño, *Mon. Wea. Rev.*, **110**, 354–384.

Rasmusson, E.M., X. Wang, and C.F. Ropelewski, 1990: The biennial component of ENSO variability. *J. Marine Syst.*, **1**, 71–96.

Robertson, A. W., 2001: On the influence of ocean-atmosphere interaction on the Arctic Oscillation in two general circulation models. *J. Climate,* **14**, 3240–3254.

Robertson, A. W., and C. R. Mechoso, 1998: Interannual and decadal cycles in river flows of southeastern South America. *J. Climate,* **11**, 2570–2581.

Robertson, A. W., C. R. Mechoso, and N. O. Garcia, 2001: Interannual prediction of the Parana River. *Geophys. Res. Lett*., **28**, 4235–4238.

Rodwell, M. J., and B. J. Hoskins, 1996: Monsoons and the dynamics of deserts, *Q. J. Roy. Meteorol. Soc*., **122**, 1385–1404.

Rogers, J. C., 1984: The association between the North Atlantic oscillation and the Southern Oscillation in the Northern Hemisphere. *Mon. Wea. Rev.,* **112**, 1999–2015.

Rogers J. C., 1990: Patterns of low-frequency monthly sea-level pressure variability (1899–1986) and associated wave cyclone frequencies. *J. Climate*, **3**, 1364-1379.

Ropelewski, C. F., and M. S. Halpert, 1987: Global and regional scale precipitation patterns associated with the El Niño/Southern Oscillation. *Mon. Wea. Rev.,* **115,** 1606–1626.

Ropelewski, C.F., and M.S. Halpert, 1989: Precipitation patterns associated with the high-index phase of the Southern Oscillation. *J. Climate,* **2,** 268–284

Ropelewski, C.F., and P.D. Jones, 1987: An extension of the Tahiti-Darwin Southern Oscillation Index. *Mon. Weather Rev.*, **115**, 2161–2165.

Rosenblum, M. G., A.S. Pikovsky, and J. Kurths, 1996: Phase synchronization of chaotic oscillators, *Phys. Rev. Lett*., **76**, 1804–1807.

Rössler, O. E., 1976: An equation for continuous chaos, *Phys. Lett.*, **57A** (5), 397–398.

Simonnet, E., M. Ghil, and H. A. Dijkstra, 2005: Homoclinic bifurcations in the quasi-geostrophic double-gyre circulation, *J. Mar. Res.*, **63**, 931–956.

Suselj and Bergant (2006) dealing with MOI indicate that the correlation between MOI and NAOI and PRC (precipitation anomalies is negative above all Mediterranean region. Geophysical Res. Abstract, 8, 02145, Sref-ID:1607-7962/gra/EGU06-A-02145.

Sushama, L., M. Ghil, and K. Ide, 2007: Spatio-temporal variability in a mid-latitude ocean basin subject to periodic wind forcing. *Atmosphere-Ocean*, **45**, 227–250, doi: 10.3137/ao.450404.

Thompson, D. W. J, and D. W. Lorenz, 2004: The signature of the annular modes in the tropical troposphere. *J. Climate,* **17,** 4330-4342.

Trenberth, K. E., and D. A. Paolino Jr., 1981: Characteristic patterns of variability of sea level pressure in the Northern Hemisphere. *Mon. Wea. Rev.*, **109**, 1169–1189.

Unal, Y. S., and M. Ghil, 1995: Interannual and interdecadal oscillation patterns in sea level, *Climate Dyn.*, **11**, 255–278.

Walker, G., 1931: On periodicity in series of related terms. *Proc. Roy. Soc. (London) Ser. A*, **131**, 518–532.

Walker, G. T., and E. W. Bliss, 1932: World Weather V. *Mem. Roy. Meteor. Soc.*, **4**, 53–84.

Walker, G. T., and E. W. Bliss, 1937: World Weather VI. *Mem. Roy. Meteor. Soc.*, **4,** No. 39, 119–139.

Wallace, J. M., and D. S. Gutzler, 1981: Teleconnections in the geopotential height field during the Northern-Hemisphere winter. *Mon. Wea. Rev.*, **109**, 784–812.

Wang, G., and E. A. B. Eltahir, 1999. Use of ENSO information for medium- and long-range forecasting of the Nile floods. *J. Climate*, **12**, 1726–1737.

Wang, W., B. T. Anderson, R. K. Kaufmann, and R. B. Myneni, 2004: The Relation between the North Atlantic Oscillation and SSTs in the North Atlantic Basin. *J. Climate*, 17, 4752-4759.

Wunsch, C., 1999: The interpretation of short climate records, with comments on the North Atlantic and Southern Oscillations, *Bull. Am. Meteorol. Soc.*, **80**, 245–255.

List of Figures

FIG. 1: The raw time series of x_1 and x_2 for two coupled Rössler oscillators; panels (a,b.c) correspond to three values of the coupling parameter C = 0.017, 0.035 and 0.120. No SSA pre-filtering is required, since the oscillations are quite regular.

FIG. 2: The climate records used in this study. (a)–(c) Climate proxies for the Eastern Mediterranean: (a) the high-water Nile record, 1825–1972, is a proxy for the Ethiopian Plateau's climate; (b) tree-ring widths of *Quercus Infectoria* from the Golan Heights, 1757–1967; and (c) annual record of total rainfall from Jerusalem, 1861–1994. (d) Monthly values of the North Atlantic Oscillation (NAO) index, 1823–2000,

Fig. 3: Spectral analysis of the detrended time series of Jerusalem precipitation. (a) Monte Carlo SSA (MC-SSA) spectrum computed with a window width of M = 45 years; the variance of each mode in the data is in red, while lower and upper ticks on the error bars indicate the 5th and 95th percentiles of a red-noise process constructed from a surrogate data ensemble of 100 series, each with the same variance and lag-one autocorrelation as the original record. The surrogate time series (Allen and Smith, 1996) were produced by projecting the first 10 principal components of the SSA analysis onto the basis vectors of a red-noise process, with M = 45 year. (b) MTM spectrum computed with 3 tapers and spectral resolution of 0.03 cycles/year; the nearly parallel curves indicate the estimated red-noise background (lowest curve, green) and associated 50%, 90%, 95%, and 99% (highest curve, red) significance levels.

FIG. 4: The high-water Nile River records. (a) Comparison between the observed nilometer record at Rhoda Island, normalized by its maximum of 4.45 m (solid line) and

the estimated high-water record — derived by linear regression, cf. Eq. (6) — from the mean annual volume flow measured at Aswan (dashed line); shown for the time interval of overlap, 1869–1922. (b) The two-channel M-SSA spectrum of the extended and detrended Nile River record (channel 1) and the NAO index for the month of August, together with a Monte Carlo significance test for the oscillations; same procedure and conventions as in Fig. 3a, except variances in black.

FIG. 5: The RC pairs that capture the oscillatory modes of the two-channel M-SSA for the Nile River record and the NAO index. The header of each panel is the period of the mode, in decreasing order of period length; channel 1 = Nile River (solid line), channel 2 = NAO index (dashed line).

FIG. 6: Humidity supply tracks leading to the Ethiopian Plateau during summer. (a) Climatological mean map of moisture fluxes and divergence for the month of August, showing vectors of humidity fluxes averaged over the 1000–850 hPa layer, together with the flux divergence (shaded, mm/day), constructed from daily NCEP-NCAR reanalysis data, over the interval 1950–2007. (b) Schematic diagram of the three moisture tracks, labeled in the circles placed at track initiation from (1) to (3).

FIG. 7: Synchronization study of the NAO index (channel 1) and Jerusalem rainfall (channel 2). (a) The M-SSA spectrum of the detrended NAO index and Jerusalem precipitation data, along with the Monte Carlo significance test for the oscillatory modes. (b) The reconstruction of the 7.8-year mode of the M-SSA; NAO index (solid), Jerusalem rainfall (dashed). (c) Same as panel (b), for the 3.8-year mode.

FIG. 8: The RC of the 12.5-year oscillatory mode of the joint spectra between the tree rings and Jerusalem rainfall; tree rings (solid), Jerusalem rainfall (dashed).

FIG. 9: Synthetic noisy time series; see Eqs. (7a, b) in appendix A. (a) Two noise-perturbed, frequency-modulated harmonic signals, $f_1(t)$ and $f_2(t)$, with the same mean period; and (b) the leading RC pair that captures the joint oscillatory mode of the two-channel SSA for $f_1(t)$ and $f_2(t)$, as given in panel (a). (c) Same as (a) but for a pair of signals that have distinct, incommensurable periods; (d) same as (b), but for the pair of signals plotted in panel (c).

Table 1: The degree of synchronization between the first components $x_1(t)$ and $x_2(t)$ of the two coupled Rössler oscillators in Eq. (5); see text for details. The columns in the table give the variance of the first reconstructed-component (RC) pair (1,2) and of the second pair (3,4); the energy ratio $\varepsilon_{12} = E(\mathrm{RC}x_1)/E(\mathrm{RC}x_2)$ between the two components of the first RC pair; the standard deviation σ of the phase differences $d(t) = \phi_1(t) - \phi_2(t)$, and the correlation of the amplitudes A_1 and A_2 of x_1 and x_2.

Coupling parameter	Variance (%) in pair		$E(\mathrm{RC}x_1)/E(\mathrm{RC}x_2)$ in pair	σ	Amplitude correlation
C	(1,2)	(3,4)	(1,2)		
0.000	51	35	0.0	46.80	– 0.07
0.001	48	41	0.02	40.02	0.01
0.005	50	41	0.6	36.68	0.02
0.01	54	38	0.76	35.07	– 0.03
0.017	62	31	1.14	30.08	– 0.11
0.025	73	21	1.11	18.21	– 0.01
0.027	86	9	1.11	7.92	– 0.08
0.035	93	1.2	1.07	0.20	0.24
0.04	93	1.2	0.93	0.19	0.28
0.06	93	1.5	0.97	0.14	0.66
0.1	93	1.6	1.00	0.09	0.88
0.11	92	1.8	1.00	0.06	0.98

Table 2: Significant oscillatory modes in climatic records. The main entries give the periods in years: entries without brackets indicate that the mode is significant at the 95% level against a null hypothesis of red noise, in both SSA and MTM results; entries in square brackets are significant at this level only in the SSA analysis. Entries in parentheses provide the percentage of variance captured by the mode with the given period.

Jerusalem rain	Tree rings	Nile River	NAO index	
			Winter (DJFM)	August
[14] (10%)	14 (20%)			
7.8 (7%)	7.7 (6%)	7.3 (4%)	7.8 (11%)	7.7 (9%)
			5.5 (7%)	
3.8 (13%)		4.2 (3%)		4.0 (9%)
3.1 (10%)		2.9 (3%)		3.2 (7%)
		2.3 (3%)	2.2 (3%)	

Table 3: Cross-spectral analysis of our climatic records, using M-SSA with two channels. Entries in the first column correspond to channel 1 and those in the first row to channel 2. In each cell there are three strings, separated by a comma: the first string gives the period in years of the oscillatory mode, the second string the synchronization type, and the third string is the energy ratio between channel 1 and channel 2. Oscillatory modes in the table are all significant at the 95% level or higher.

	NAO index	Jerusalem rain
Nile River	7.6y, FPA, 0.28	
Nile River	4.3y, FPA, 0.97	
Nile River	3.3y, FPA, 0.11	
Jerusalem	7.8y, FPA, 2.8	
Jerusalem	3.8y, FP, 0.8	
Tree rings		12.5y, FA, 0.70
Tree rings		7.8y, F, 0.41
Tree rings		3.8y, F, 0.01

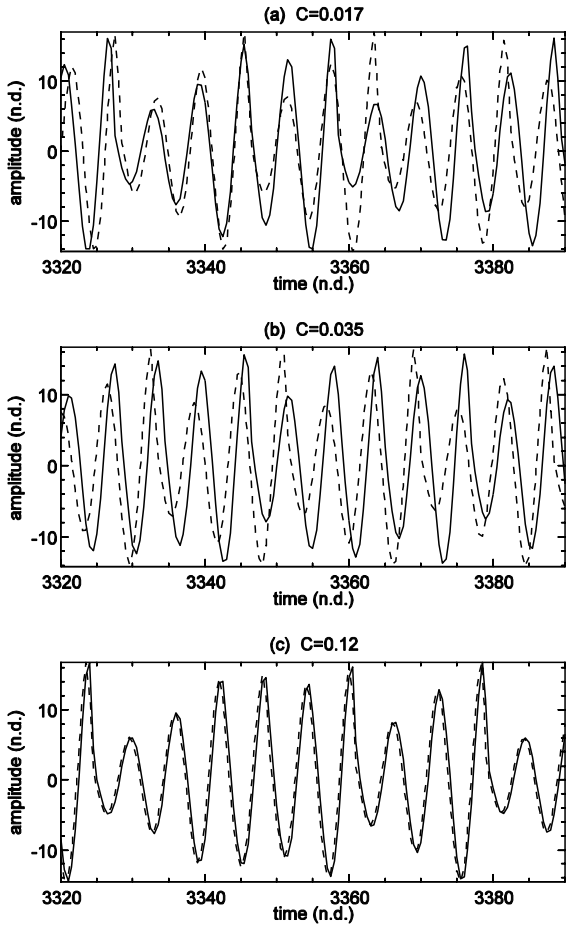

FIG. 1: The raw time series of x_1 and x_2 for two coupled Rössler oscillators; panels (a,b.c) correspond to three values of the coupling parameter C = 0.017, 0.035 and 0.120. No SSA pre-filtering is required, since the oscillations are quite regular.

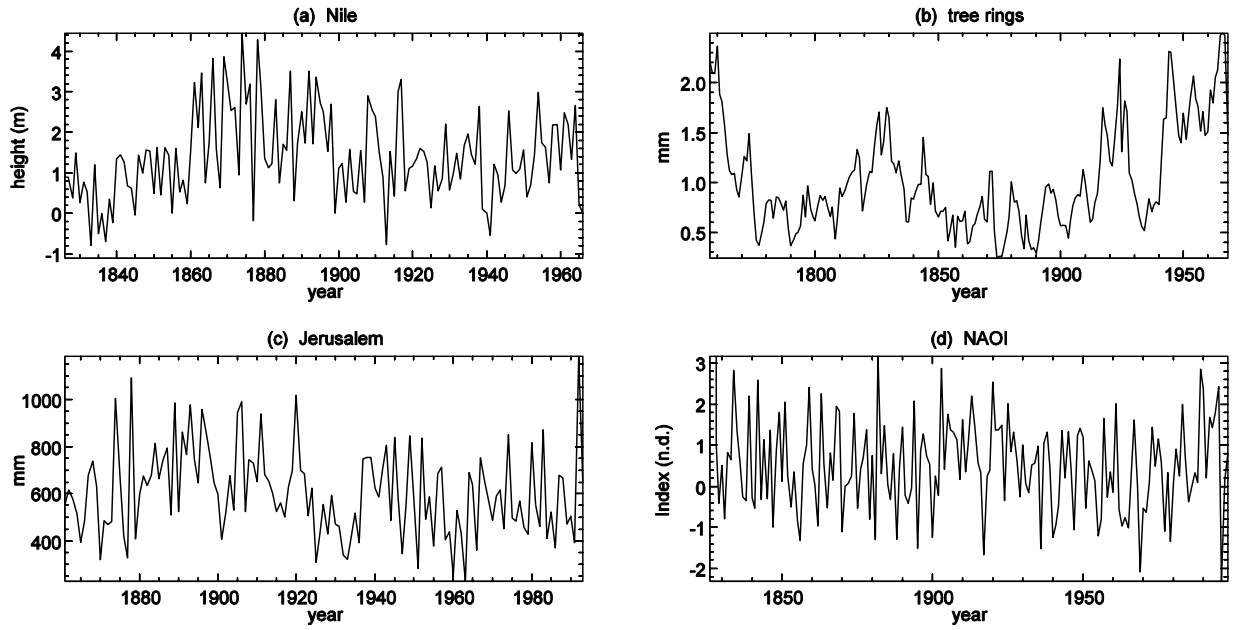

FIG. 2: The climate records used in this study. (a)–(c) Climate proxies for the Eastern Mediterranean: (a) the high-water Nile record, 1825–1972, is a proxy for the Ethiopian Plateau's climate; (b) tree-ring widths of *Quercus Infectoria* from the Golan Heights, 1757–1967; and (c) annual record of total rainfall from Jerusalem, 1861–1994. (d) Monthly values of the North Atlantic Oscillation (NAO) index, 1823–2000.

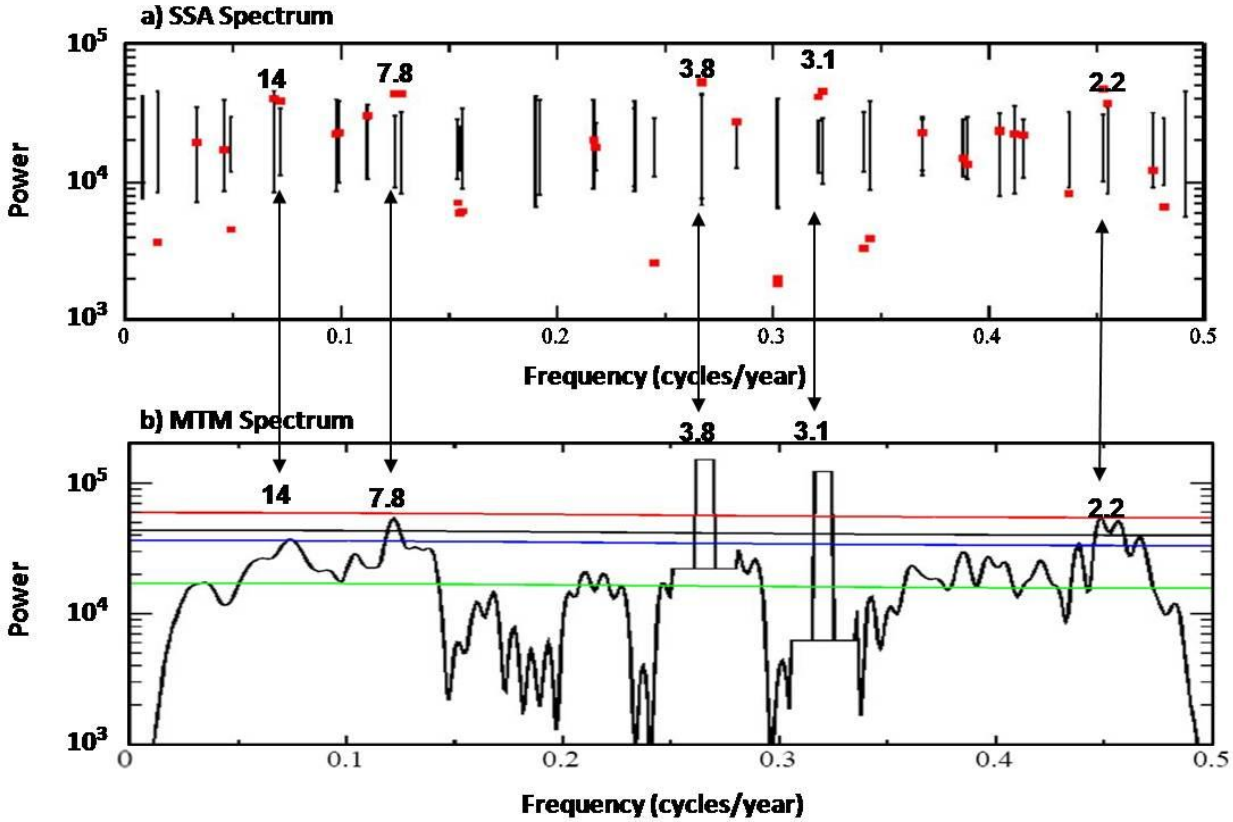

Fig. 3: Spectral analysis of the detrended time series of Jerusalem precipitation. (a) Monte Carlo SSA (MC-SSA) spectrum computed with a window width of M = 45 years; the variance of each mode in the data is in red, while lower and upper ticks on the error bars indicate the 5th and 95th percentiles of a red-noise process constructed from a surrogate data ensemble of 100 series, each with the same variance and lag-one autocorrelation as the original record. The surrogate time series (Allen and Smith, 1996) were produced by projecting the first 10 principal components of the SSA analysis onto the basis vectors of a red-noise process, with M = 45 year. (b) MTM spectrum computed with 3 tapers and spectral resolution of 0.03 cycles/year; the nearly parallel curves indicate the estimated red-noise background (lowest curve, green) and associated 50%, 90%, 95%, and 99% (highest curve, red) significance levels.

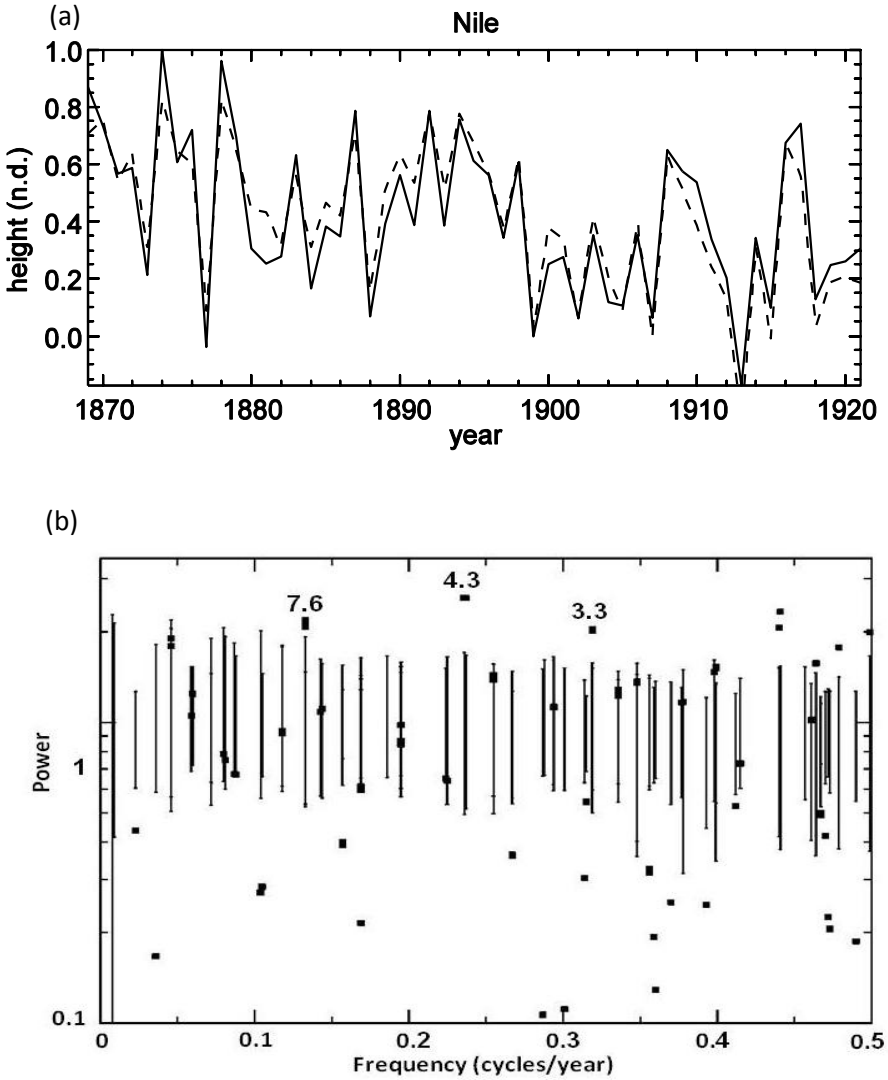

FIG. 4: The high-water Nile River records. (a) Comparison between the observed nilometer record at Rhoda Island, normalized by its maximum of 4.45 m (solid line) and the estimated high-water record — derived by linear regression, cf. Eq. (6) — from the mean annual volume flow measured at Aswan (dashed line); shown for the time interval of overlap, 1869–1922. (b) The two-channel M-SSA spectrum of the extended and detrended Nile River record (channel 1) and the NAO index for the month of August, together with a Monte Carlo significance test for the oscillations; same procedure and conventions as in Fig. 3a, except variances in black.

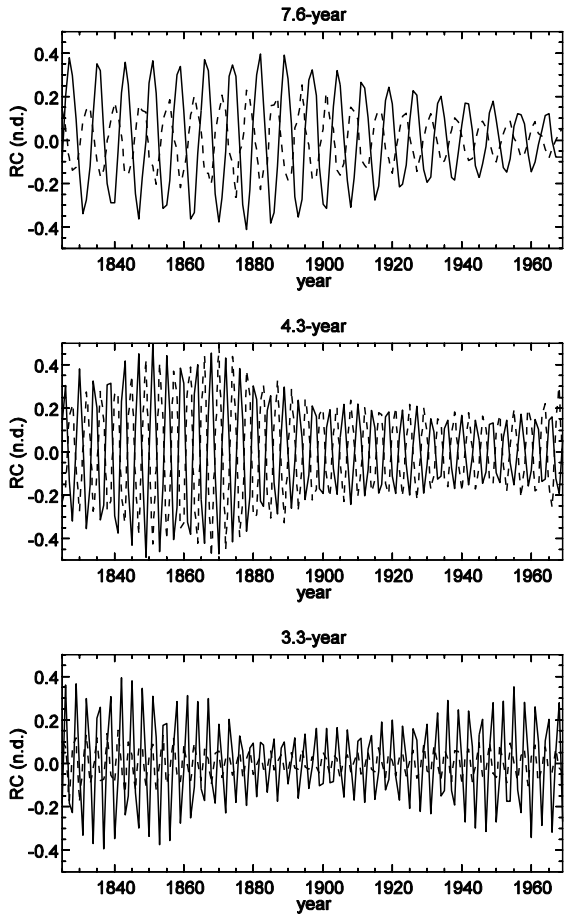

FIG. 5: The RC pairs that capture the oscillatory modes of the two-channel M-SSA for the Nile River record and the NAO index. The header of each panel is the period of the mode, in decreasing order of period length; channel 1 = Nile River (solid line), channel 2 = NAO index (dashed line).

(a)

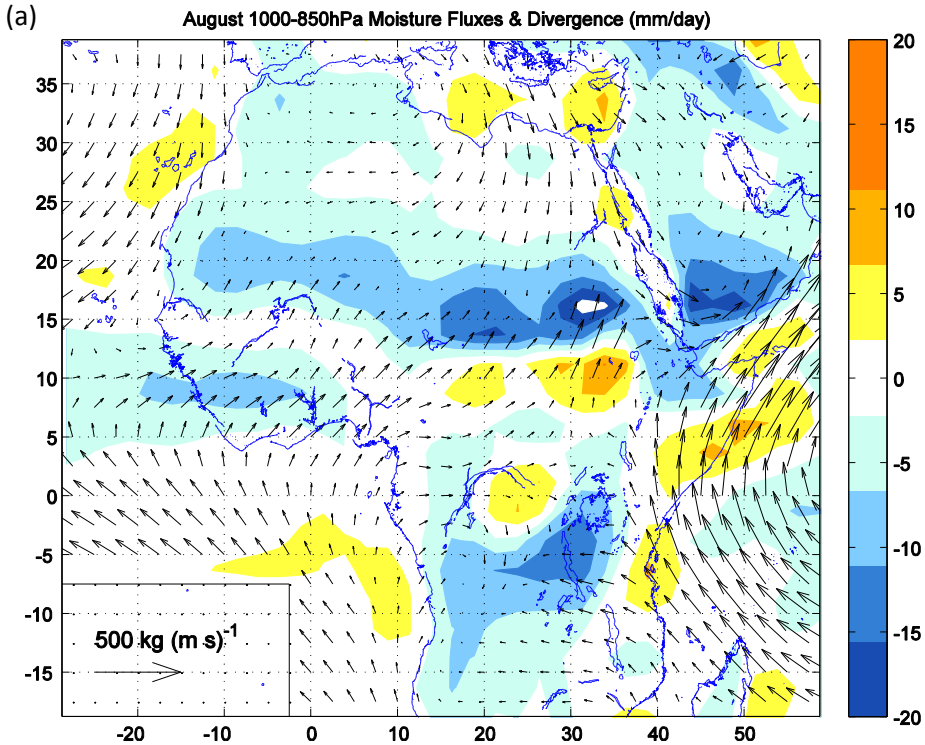

(b)

FIG. 6: Humidity supply tracks leading to the Ethiopian Plateau during summer. (a) Climatological mean map of moisture fluxes and divergence for the month of August, showing vectors of humidity fluxes averaged over the 1000–850 hPa layer, together with the flux divergence (shaded, mm/day), constructed from daily NCEP-NCAR reanalysis data, over the interval 1950–2007. (b) Schematic diagram of the three moisture tracks, labeled in the circles placed at track initiation from (1) to (3).

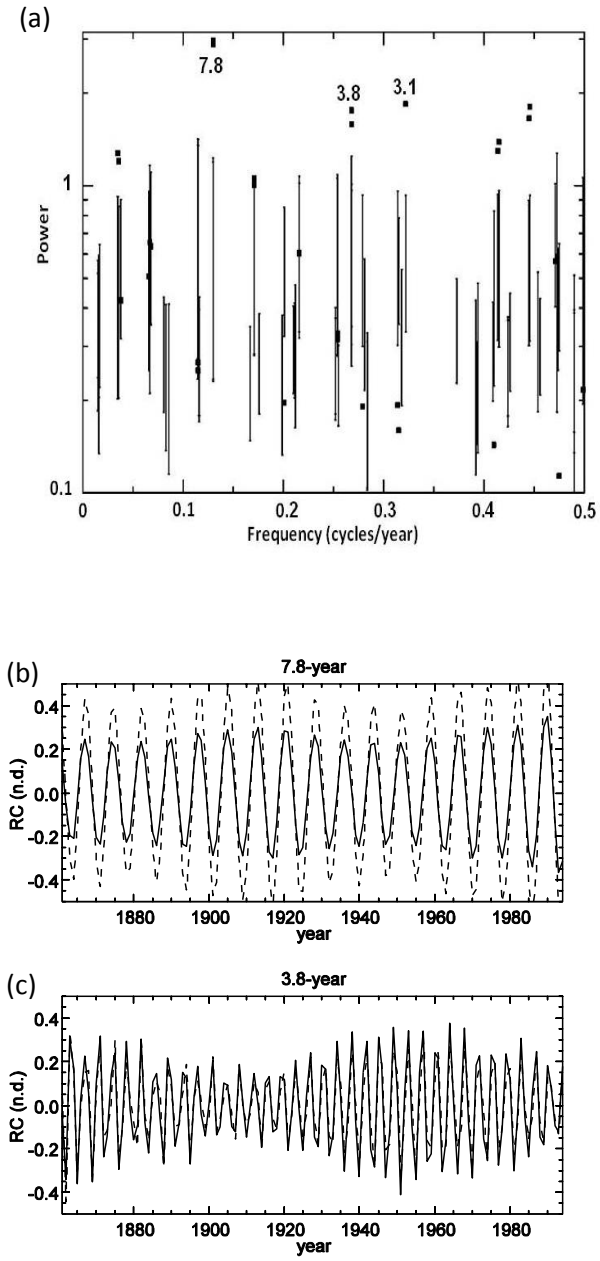

FIG. 7: Synchronization study of the NAO index (channel 1) and Jerusalem rainfall (channel 2). (a) The M-SSA spectrum of the detrended NAO index and Jerusalem precipitation data, along with the Monte Carlo significance test for the oscillatory modes. (b) The reconstruction of the 7.8-year mode of the M-SSA; NAO index (solid), Jerusalem rainfall (dashed). (c) Same as panel (b), for the 3.8-year mode.

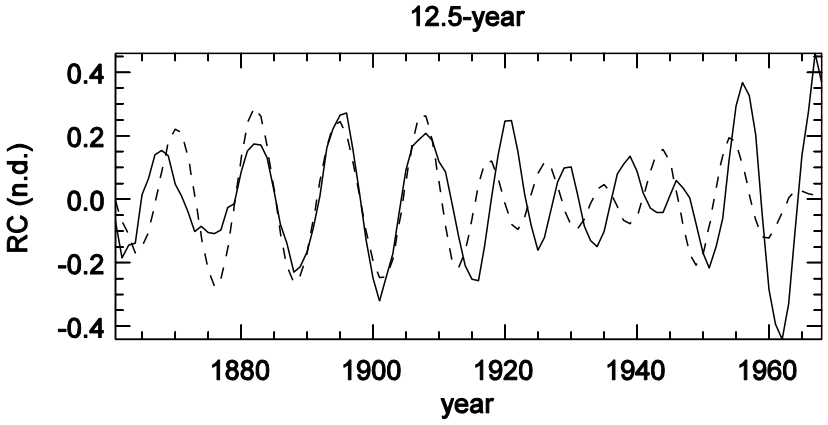

FIG. 8: The RC of the 12.5-year oscillatory mode of the joint spectra between the tree rings and Jerusalem rainfall; tree rings (solid), Jerusalem rainfall (dashed).

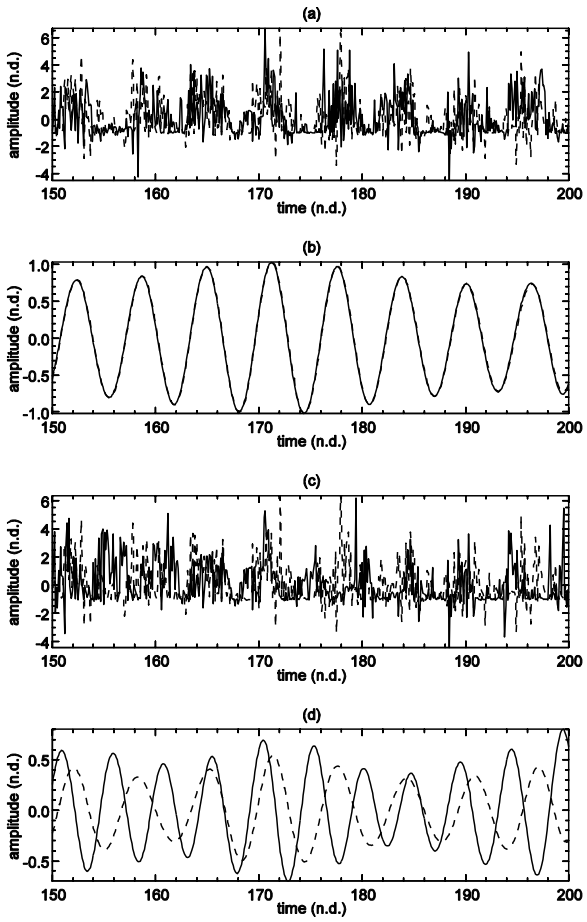

FIG. 9: Synthetic noisy time series; see Eqs. (7a, b) in appendix A. (a) Two noise-perturbed, frequency-modulated harmonic signals, $f_1(t)$ and $f_2(t)$, with the same mean period; and (b) the leading RC pair that captures the joint oscillatory mode of the two-channel SSA for $f_1(t)$ and $f_2(t)$, as given in panel (a). (c) Same as (a) but for a pair of signals that have distinct, incommensurable periods; (d) same as (b), but for the pair of signals plotted in panel (c).